ATLAS NOTE

ATLAS-CONF-2015-005

March 17, 2015

Study of the Higgs boson decaying to WW^* produced in association with a weak boson with the ATLAS detector at the LHC

The ATLAS Collaboration

Abstract

The search for Higgs boson production in association with a W or a Z boson, in the decay channel $H \to WW^*$, is performed with a data sample collected with the ATLAS detector at the LHC in proton-proton collisions at centre-of-mass energies $\sqrt{s} = 7$ TeV and 8 TeV, corresponding to integrated luminosities of 4.5 fb^{-1} and 20.3 fb^{-1}, respectively. The WH production mode is studied in three and two lepton final states, while a four lepton final state is used to search for ZH production. The observed significance is of 2.5 standard deviations while a significance of 0.9 standard deviations is expected for a Standard Model Higgs boson. The ratio of the combined WH and ZH signal yield to the Standard Model expectation, μ_{VH}, is found to be $\mu_{\text{VH}} = 3.0^{+1.3}_{-1.1}$ (stat.)$^{+1.0}_{-0.7}$ (sys.) for a Higgs boson mass of 125.36 GeV. The WH and ZH channels are also combined with the gluon-gluon fusion and vector boson fusion production modes studied in the $H \to WW^* \to \ell\nu\ell\nu$ decay channel. The results are interpreted in terms of scaling factors of the Higgs boson couplings to vector bosons (k_V) and fermions (k_F), the combined results are: $|k_V| = 1.06^{+0.10}_{-0.10}$, $|k_F| = 0.85^{+0.26}_{-0.20}$.

1 Introduction

In the Standard Model (SM) of particle physics, the Brout-Englert-Higgs [1–3] mechanism induces the electroweak symmetry breaking that results in providing mass to elementary particles. The mechanism postulates the existence of an elementary scalar particle, the Higgs boson. The ATLAS and CMS collaborations at the CERN Large Hadron Collider (LHC) have observed the Higgs boson with a mass (m_H) of about 125 GeV [4,5]. Currently the measurement of the couplings of the Higgs boson to SM particles as well as its spin and CP quantum numbers [6–12] are essential tests of the SM. Higgs boson production in association with a W or Z boson (respectively denoted as WH and ZH), which are collectively referred to as VH associated production in the following, provides direct access to the Higgs boson couplings to gauge bosons. In particular, in the WH mode with the subsequent $H \rightarrow WW^*$ decay, the Higgs boson couples only to W bosons, both at the production and decay vertices.

Production of VH has been tested both at the Tevatron [13] and at the LHC [14–20], in events with leptons and either missing transverse momentum or two central jets. No VH production has been observed so far.

In the present work, a search for Higgs boson production in association with a vector boson, with the subsequent $H \rightarrow WW^*$ decay, is presented. The analysed data were collected in the years 2011 and 2012 by the ATLAS experiment at centre-of-mass energies of $\sqrt{s}$ = 7 TeV and 8 TeV, respectively. In the SM, for m_H = 125 GeV, the cross sections of the WH and ZH associated production modes, followed by the $H \rightarrow WW^*$ decay, are 0.12 pb and 0.07 pb at $\sqrt{s}$ = 7 TeV and 0.15 pb and 0.09 pb at $\sqrt{s}$ = 8 TeV [21], respectively. Four topologies are considered, with four, three and two leptons in the final state, respectively. The analyses are optimised to search for both WH and ZH processes; a combined search for VH is also presented. The VH results are then further combined with the $H \rightarrow WW^* \rightarrow \ell\nu\ell\nu$ analysis in the gluon-gluon fusion (ggF) and vector boson fusion (VBF) production modes [22], in which the ATLAS collaboration has reported the observation of the Higgs boson in the $H \rightarrow WW^*$ decay mode with a significance of 6.1 standard deviations. The combination of the ggF, VBF and VH analyses, presented in this note, are used to determine the couplings of the Higgs boson to vector bosons and, indirectly, to fermions, providing further constraints on the Higgs boson couplings. The results are consistent with the SM predictions.

2 Analysis Overview

The Higgs boson VH production, followed by the $H \rightarrow WW^*$ decay, is searched for using events with four, three or two electrons or muons in the final state. Leptonic decays of tau leptons from $H \rightarrow WW^* \rightarrow \tau\nu\tau\nu$ are included in the analysed sample and they are considered as signal, but no specific selection is considered for events with hadronically decaying tau leptons in the final state. The analysis selection is designed to select events whose kinematic is consistent with the VH signal for each final state, in order to enhance the signal to background ratio. Figure 1 illustrates the relevant tree-level diagrams of the studied processes, in which a Higgs boson is produced in association with a gauge boson (W or Z).

Four channels are analysed, defined as follows:

(a) **4ℓ channel** (Figure 1a): The leading contribution consists of a process in which a virtual Z boson radiates a Higgs boson, which in turn decays to a W boson pair. The decays of the gauge bosons produce four charged leptons and two neutrinos in the final state. The lepton pair with an invariant mass closest to the Z-boson mass is labelled as (ℓ_2, ℓ_3), while the remaining leptons are labelled as ℓ_0 and ℓ_1 and are assumed to originate in the $H \rightarrow WW^*$ decay. Main backgrounds to this channel are the non-resonant ZZ^* and ZWW^* production.

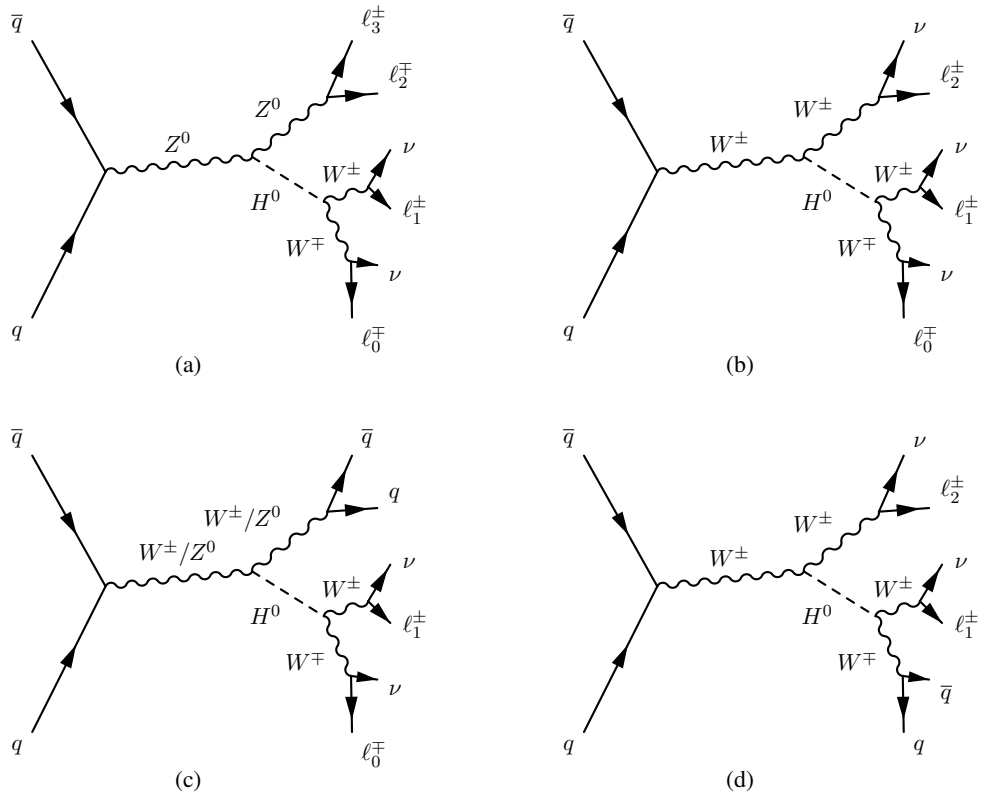(b) **3ℓ channel** (Figure 1b): The leading contribution consists of a process in which a virtual W boson

Figure 1: Feynman diagrams at tree-level of the *VH* topologies studied in the present analysis: (a) 4ℓ channel (b) 3ℓ channel (c) opposite-sign 2ℓ channel and (d) same-sign 2ℓ channel.

radiates a Higgs boson, and the Higgs boson decays to a W boson pair. All the gauge bosons decay leptonically producing three charged leptons and three neutrinos in the final state. The lepton with unique charge is labelled as ℓ_0, the lepton closest to ℓ_0 in angle is labelled as ℓ_1, and the remaining lepton is labelled as ℓ_2. Leptons ℓ_0 and ℓ_1 are assumed to be produced by the $H \to WW^*$ decay. The most prominent background to this channel is $WZ/W\gamma^*$ production; non-resonant WWW^* production is also a significant background and has the same final state as the signal. ZZ^*, $Z\gamma$, Z+jets, $t\bar{t}$ and Wt production are also important backgrounds, as they mimic the signal selection if a lepton is undetected or because of a fake or non-prompt lepton from a jet.

(c) **Opposite-sign** 2ℓ **channel** (Figure 1c): The leading contribution consists of a process in which the vector boson V, which radiates the Higgs boson, decays hadronically producing two energetic jets, while the W bosons from the $H \to WW^*$ decay produce two oppositely charged leptons, labelled as ℓ_0 and ℓ_1, and two neutrinos. The WH process is expected to account for 70% of the signal yield, while the ZH process accounts for the remaining 30%. The leading backgrounds for this channel are $t\bar{t}$ and Wt. $Z \to \tau\tau$ and WW production with two associated jets are also major components. Final states including W+jets and multijets may produce fake leptons, contaminating the signal region. Other background sources include $WZ/W\gamma^*$ production and other Higgs boson production modes, including ggF production.

(d) **Same-sign** 2ℓ **channel** (Figure 1d): The leading contribution consists of a process in which both the W boson, produced in association with the Higgs boson, and one of the W bosons from the Higgs boson decay leptonically. Only final states with same-sign leptons are selected. The third W boson decays hadronically. The final state therefore contains two same-sign leptons, labelled as ℓ_1 and ℓ_2, two neutrinos and two energetic jets. Significant backgrounds in this channel are $WZ/W\gamma^*$, $W\gamma$ and W+jets production. WW, Z+jets and top-quark processes also contribute. The selection is not optimised for events in which the lepton from the Higgs boson decay has opposite charge with respect to the lepton from the associated W due to the overwhelming background from the $t\bar{t}$ production.

All the channels described above are mutually exclusive based on the number of leptons with $p_T >$ 15 GeV. With the exception of the opposite-sign 2ℓ channel, all topologies are further subdivided into several signal regions (SRs) to enhance the analysis sensitivity. The 4ℓ channel is split into two samples according to the number of same-flavor opposite-sign (SFOS) lepton pairs. The sample containing two SFOS pairs suffers from a higher background contamination than the sample with one SFOS pair. The 3ℓ analysis separates events with at least one pair of SFOS leptons from events without any SFOS pair. The sample with at least one SFOS pair is further split into two subsamples, with one and two SFOS pairs, which have different signal to background ratios. In these signal regions a multivariate analysis is performed. The same-sign 2ℓ sample is divided into two sub-channels with one (SS1jet) or two (SS2jet) selected jets in the final state. Additional data samples are defined in order to normalise the major backgrounds in each channel; they are referred to as control regions (CR) in the following. The final results are extracted from a fit simultaneously performed on all SRs and CRs. The channel with two leptons of different-flavour and opposite-sign is denoted as 2ℓ-DFOS in the following sections.

3 The ATLAS Detector

ATLAS [23] is a multi-purpose particle physics detector with a forward-backward symmetric cylindrical geometry[1] and near 4π coverage in solid angle. It consists of an inner tracking detector (ID) surrounded

---

[1] ATLAS uses a right-handed coordinate system with its origin at the nominal interaction point (IP) in the centre of the detector and the z-axis along the beam pipe. The x-axis points from the IP to the centre of the LHC ring, and the y axis points

by a thin 2 T superconducting solenoid, electromagnetic and hadronic calorimeters, and a muon spectrometer (MS) incorporating three large superconducting toroid magnets of eight coils each.

The ID covers pseudorapidities up to $|\eta| = 2.5$ and consists of multiple layers of silicon pixel and strip detectors, and a straw-tube transition radiation tracker. The calorimeter system covers the pseudorapidity range $|\eta| < 4.9$. Within the region $|\eta| < 3.2$, electromagnetic calorimetry is provided by barrel and endcap high-granularity lead/liquid-argon (LAr) calorimeters. An additional thin LAr presampler covering $|\eta| < 1.8$ is used to correct for energy loss in the material upstream of the calorimeters. Hadronic calorimetry is provided by a steel/scintillating-tile calorimeter, covering $|\eta| < 1.7$, and two copper/LAr hadronic endcap calorimeters. The solid angle coverage is completed with forward copper/LAr and tungsten/LAr calorimeter modules optimised for electromagnetic and hadronic measurements, respectively. The MS consists of separate trigger and high-precision tracking chambers that measure the deflection of muons in the magnetic field generated by superconducting air-core toroids. The precision chamber system covers the region $|\eta| < 2.7$ with three stations of monitored drift tube layers, except for the forward region where the innermost station is equipped with cathode strip chambers. The muon trigger system covers the range $|\eta| < 2.4$ with resistive plate chambers in the barrel and thin gap chambers in the endcap regions. A three-level trigger system is used. The first-level trigger is hardware-based, using a subset of the detector information, and reduces the event rate below 75 kHz. This is followed by two software-based trigger levels, which together reduce the event rate to about 300 Hz.

4 Data Samples

The analysed data were recorded using inclusive single-lepton and dilepton triggers. Overall quality criteria are applied in order to suppress non-collision backgrounds such as cosmic-ray muons, beam-related backgrounds, or noise in the calorimeters. The datasets used in the 7 TeV and 8 TeV analyses correspond to an integrated luminosity of 4.5 fb^{-1} and 20.3 fb^{-1}, respectively. The analysis of the same-sign 2ℓ channel has been performed only on the 8 TeV data sample. The 8 TeV data were taken at a higher instantaneous luminosity ($\mathcal{L} \simeq 7 \times 10^{33}$ cm^{-2}s^{-1}) than that for the 7 TeV data ($\mathcal{L} \simeq 3 \times 10^{33}$ cm^{-2}s^{-1}) but with a higher number ($\simeq 21$ versus $\simeq 9$) of overlapping proton-proton collisions (pile-up). The increased pile-up rate, rather than the increased centre-of-mass energy, is the main reason for the differences between 7 TeV and 8 TeV analysis selections.

Table 1 lists the Monte Carlo (MC) generators and the cross sections that have been used to model and normalise the signal and background processes.

The Higgs boson production cross-sections are quoted at a Higgs boson mass of 125 GeV. The matrix-element-level calculations are interfaced to generators that are able to model the parton shower, the hadronisation and the underlying event, using either PYTHIA6, PYTHIA8, HERWIG (with the underlying event modeled by JIMMY [24]), or SHERPA. The CT10 parton distribution function (PDF) set [25] is used for the POWHEG and SHERPA samples while CTEQ6L1 [26] PDF set is used for ALPGEN+HERWIG and ACERMC samples. The $Z/\gamma^{(*)}$ sample is reweighted to the MRSTMCal [27] PDF set. The simulated samples are described in detail in the paper on the $H \to WW^*$ decay mode [22] with a few exceptions that are reported in the following. The VH signal samples are normalised to the next-to-leading order (NLO) QCD calculations [21,28–31] with additional NLO electroweak (EW) corrections applied as a function of the transverse momentum, p_T, of the associated vector boson using calculations by HAWK [32]. The $gg \to ZH$ signal samples are normalised to the next-to-next-to-leading order (NNLO) QCD calculations [29]. The associated Higgs boson production with a $t\bar{t}$ pair ($t\bar{t}H$) is simulated with PYTHIA8 and normalised to the NLO QCD estimation [21, 28, 29].

---

upward. Cylindrical coordinates (r, ϕ) are used in the transverse plane, ϕ being the azimuthal angle around the beam pipe. The pseudorapidity is defined in terms of the polar angle θ as $\eta = -\ln\tan(\theta/2)$.

The Z/γ^* processes associated with light and heavy flavour (HF) jets are modelled by Alpgen+Herwig with merged leading order (LO) calculations. The simulation includes processes with up to five additional partons in the matrix element (or three additional partons in processes with b or c-quarks). An overlap removal procedure is applied to avoid double counting of heavy flavours in the light jet samples. The sum of the two samples is normalised to the NNLO calculation of Dynnlo [33, 34]. The $t\bar{t}W/Z$ and tZ backgrounds are simulated using Madgraph at LO interfaced with Pythia6. The production of four leptons from a pair of virtual Z or γ bosons (indicated as ZZ^* in the following) contributes to the background of the 3ℓ channel when one low-p_T lepton is not detected. Since this background is more prominent when one lepton pair has a very low mass, a dedicated sample which requires at least one SFOS pair with $m_{\ell\ell} < 4$ GeV, generated with Sherpa and normalised to the NLO QCD cross section from MCFM [35], is included. Production of triboson processes is a major source of background, in particular WWW^* in the 3ℓ channel and ZWW^* in the 4ℓ channel. They are modelled by Madgraph interfaced with Pythia6 and normalised to the NLO cross section from Ref. [36].

All samples are processed using the full ATLAS detector simulation [37] based on Geant4 [38], except for WH, $WZ/W\gamma^*$ with $m_{\ell\ell} > 7$ GeV, $q\bar{q}/qg \to WW$, $WW\gamma^*$, $t\bar{t}$ and single top, which are instead simulated with Atlfast-II [37], a parametrisation of the response of the electromagnetic and hadronic calorimeters, and with Geant4 for other detector components [39]. The events are reweighted to ensure that the distribution of the number of interactions per bunch crossing is correctly reproduced.

5 Event Reconstruction and Selection

5.1 Event Reconstruction

Muons are reconstructed over the region $|\eta| < 2.5$ by combining tracks reconstructed in the MS and the ID [51]. Electrons are identified within the region $|\eta| < 2.47$, except in the boundary region between barrel and endcap calorimeters ($1.37 < |\eta| < 1.52$), through the association of an ID track to a calorimeter cluster whose shower profile is consistent with an electromagnetic shower [52]. The electron identification exploits both calorimeter and track quantities, through a cut-based approach in the 7 TeV analysis and a likelihood-based selection in the 8 TeV analysis [53].
Both track-based and calorimeter-based isolation cuts are applied on leptons. The isolation criteria are optimised to maximise the sensitivity to VH production at $m_H = 125$ GeV. The track-based isolation is built on the computation of the scalar sum of the transverse momenta of tracks associated to the primary vertex belonging to a cone, constructed around the candidate lepton, of size $\Delta R = 0.2$, where $\Delta R = \sqrt{\Delta\eta^2 + \Delta\phi^2}$. The calorimeter isolation is based on the scalar sum of the transverse energies measured within a cone of $\Delta R = 0.2$, excluding the energy of the calorimeter cluster associated with the particle itself. For the 8 TeV data the electron calorimeter isolation algorithm is based on topological clusters [53], while for the 7 TeV data it is based on calorimeter cells. Cells are used for the isolation for muon tracks in the calorimeter in both 7 and 8 TeV data. The calorimeter and track isolation criteria vary between the 7 and 8 TeV data samples and are not the same for all the analyses presented here. The upper cut applied on the threshold of the calorimeter energy varies from 7% to 30% of the lepton E_T, while the sum of the p_T values of the tracks in the cone cannot exceed values between 4% to 12% of the lepton p_T. Less stringent isolation criteria on energy and p_T are required for the 7 TeV data sample.

Jets are reconstructed from three-dimensional topological clusters [54] over the region $|\eta| < 4.5$ using the anti-k_t algorithm [55] with radius parameter $R = 0.4$. They are required to have p_T larger than 25 GeV except for the forward region, $|\eta| > 2.4$, in which the threshold is raised to 30 GeV. In order to suppress the contamination of jets from pile-up, a special selection is applied: the sum of the p_T of all tracks in the jet within $\Delta R = 0.4$ and that of the subset of these associated to the primary vertex is computed. For the 8 TeV data sample, the ratio between the second and the first of these two quantities is required to be

Process	Generator	$\sigma \times$ Br [pb]	Cross section normalisation
Higgs			
VH $(H \to WW^*)$	Pythia [40] v8,v6	0.25, 0.20	NNLO QCD + NLO EW
VH $(H \to \tau\tau)$	Pythia [40] v8,v6	0.07, 0.06	NNLO QCD + NLO EW
$gg \to H$ $(H \to WW^*)$	Powheg [41] + Pythia v8, v6	0.44, 0.34	NNLO QCD + NLO EW
VBF $(H \to WW^*)$	Powheg + Pythia v8, v6	0.035, 0.027	NNLO QCD + NLO EW
$t\bar{t}$H $(H \to WW^*)$	Pythia v8	0.028, 0.023	NLO
Single boson			
Z/γ^*+jets $(m_{\ell\ell} > 10$ GeV)	Alpgen [42] + Herwig [43]	16540, 12930	NNLO
HF Z/γ^*+jets $(m_{\ell\ell} > 30$ GeV)	Alpgen + Herwig	126, 57	NNLO
VBF Z/γ^* $(m_{\ell\ell} > 7$ GeV)	Sherpa [44]	5.3, 2.8	LO
Top-quark			
$t\bar{t}$	Powheg+Pythia v6, MC@NLO [45]	26.6, 18.6	NNLO
$t\bar{t}W/Z$	MadGraph4 [46], 5 [47] +Pythia v6	0.35, 0.25	LO
tqb	AcerMC [48] +Pythia v6	28.4, 20.9	NNLL
tb, tW	Powheg + Pythia v6	4.17, 3.15	NNLL
tZ	MadGraph4, 5+Pythia v6	0.035, 0.025	LO
Dibosons			
$WZ/W\gamma^*(m_{\ell\ell} > 7$ GeV)	Powheg +Pythia v8, v6	12.7, 10.7	NLO
$WZ/W\gamma^*$(min. $m_{\ell\ell} < 7$ GeV)	Sherpa	12.2, 10.5	NLO
$q\bar{q}/qg \to Z^{(*)}Z^{(*)}$ $(m_{\ell\ell} > 4$ GeV)	Powheg+Pythia v8, v6	1.24, 0.79	NLO
$q\bar{q}/qg \to Z^{(*)}Z^{(*)}$ (min. $m_{\ell\ell} < 4$ GeV)	Sherpa	7.3, 5.9	NLO
$gg \to Z^{(*)}Z^{(*)}$	gg2ZZ [49] + Herwig (8 TeV only)	0.0027	LO
$q\bar{q}/qg \to WW$	Powheg + Pythia v6	5.68, 4.68	NLO
	Sherpa (for 2ℓ-DFOS 8 TeV only)	5.68	NLO
$gg \to WW$	gg2WW [50] + Herwig	0.20, 0.120	LO
VBS WZ, ZZ $(m_{\ell\ell} > 7$ GeV), WW	Sherpa	0.099, 0.037	LO
$W\gamma$ $(p_\mathrm{T}^\gamma > 8$ GeV)	Alpgen +Herwig	369, 313	NLO
$Z\gamma$ $(p_\mathrm{T}^\gamma > 8$ GeV)	Sherpa	97, 82	NLO
Tribosons			
$WWW^*, ZWW^*, ZZZ^*, WW\gamma^*$	MadGraph4, 5 + Pythia v6	0.017, 0.011	NLO

Table 1: MC generators used to model the signal and background processes. Here and in the text Powheg refers to the POWHEG-BOX generator. The Higgs boson samples are normalised using the production cross section and the decay branching fraction computed for a mass of 125 GeV. The values reported for the VH $(H \to WW^*)$ process include the NNLO contribution from the $gg \to ZH$ $(H \to WW^*)$ process. For generators and cross sections, wherever two comma-separated values are given, the first value refers to $\sqrt{s} = 8$ TeV and the second to $\sqrt{s} = 7$ TeV. When a single value is given, it refers to the $\sqrt{s} = 8$ TeV simulation. The corresponding cross section times branching fraction, $\sigma \times$ Br, includes the decays $t \to Wb$, $W^{(*)} \to e\nu$, $\mu\nu$, $\tau\nu$ and $Z^{(*)} \to ee$, $\mu\mu$, $\tau\tau$. 'HF' refers to heavy-flavour jet production, and 'VBS' refers to vector boson scattering. When a lower cut on $m_{\ell\ell}$ is specified, it is applied to all SFOS lepton pairs, while when an upper cut is indicated it is applied to at least one SFOS lepton pair in the event. Cross sections are computed to different levels of accuracy (LO, NLO, NNLO or next-to-next-to-leading-logarithm, NNLL), as specified by the last column. 2ℓ-DFOS is the channel with two leptons of different-flavour and opposite-sign.

larger than 0.5 for all jets with $p_T < 50$ GeV and $|\eta| < 2.4$. For the 7 TeV data the threshold is increased to 0.75 for all jets with $p_T < 50$ GeV and $|\eta| < 2.4$.

The MV1 b-jet identification algorithm is used to tag jets containing a b-hadron [56]. For b-jets with $|\eta| < 2.5$ and $p_T > 20$ (25) GeV in the 8 (7) TeV data analysis, the selection has an efficiency of 85%, estimated using simulated $t\bar{t}$ events. It corresponds to a rejection of a factor 10 against jets originating from light quarks or gluons [57, 58].

When two leptons are reconstructed within a cone of $\Delta R = 0.1$, or a lepton and a jet are reconstructed within $\Delta R = 0.3$, they are considered to be the same physical object and the duplication of reconstructed objects is resolved according to well defined priorities. In the presence of the overlap between two leptons of the same flavour, the highest p_T object is kept while the lower p_T object is ignored. The muon is kept in presence of an overlap with an electron, the electron is kept in presence of an overlap with a jet, and the jet is kept in presence of an overlap with a muon.

Two variables describing the missing transverse momentum are calculated in this analysis: one is calorimeter-based and the other is track-based. The first one, which benefits from the large rapidity coverage of the calorimeter and its sensitivity to neutral particles, is referenced as $\mathbf{E}_T^{miss}$ in the following [59]. The $\mathbf{E}_T^{miss}$ magnitude (E_T^{miss}) is used in the analysis selection. The quantity $\mathbf{E}_T^{miss}$ is calculated as the negative vector sum of the momenta of muons, electrons, taus, photons, jets and clusters of calorimeter cells that are not associated with these objects (the "soft-term"). In the 8 TeV analysis, to suppress the pile-up effect, the soft-term is scaled by the ratio of the summed scalar p_T of tracks from the primary vertex not matched with objects to the summed scalar p_T of all tracks in the event also not matched to objects [60]. The track-based missing transverse momentum measurement is used to reduce the effects of the pile-up on the resolution of the calorimeter-based variant [61]. It is obtained as vector sum of tracks with $p_T > 500$ MeV that originate from the primary vertex. This quantity is called $\mathbf{p}_T^{miss}$, and the analysis selections are applied on its magnitude, p_T^{miss}. In order to include neutral components in the calculation for final states with jets, the sum of track momenta in jets is replaced by their energy measured in the calorimeter.

5.2 Event Selection

Selected events must contain a primary vertex with at least three well-reconstructed charged particle tracks associated to it, each with $p_T > 400$ MeV. If there is more than one primary vertex reconstructed in the event, the vertex of the hard interaction is identified by computing the sum of the p_T^2 of the tracks associated to it; the vertex with the largest value is selected.

The four analysed channels are further split into eight signal regions, designed to optimise the sensitivity to the VH production, with a specific set of cuts applied to define each signal region. The selection criteria rely on the number of leptons and their properties such as charge, flavour, transverse momentum, and on the number of jets and b-jets and amount of missing transverse momentum. Of particular importance are the invariant masses and opening angles among the selected objects, most notably those of opposite-sign lepton pairs. The spin-0 nature of the Higgs boson, in conjunction with the V-A nature of the weak interaction, results in a preference for a small opening angle for lepton pairs from $H \to WW^* \to \ell\nu\ell\nu$ decays. On the other hand, as described in section 2, major backgrounds often contain Z boson production or $t\bar{t}$ production which give rise to opposite-sign lepton pairs with a large opening angle. In the same-sign 2ℓ channel, the lepton decay product of the Higgs boson candidate is selected by choosing the lepton with the smallest opening angle with respect to the jet(s); cuts are therefore applied to the opening angle and to the invariant mass between this lepton and the jets. The definitions of the signal regions used for each channel are summarised in Table 5.2 and further detailed in sections 5.2.1- 5.2.4.

In all the 4ℓ and 3ℓ signal regions, events are recorded using inclusive single lepton triggers, which are fully efficient for high lepton multiplicity signatures, while for the 2ℓ channels in 8 TeV data taking

Channel	4ℓ		3ℓ			2ℓ		
Category	2SFOS	1SFOS	2SFOS	1SFOS	0SFOS	DFOS	SS2jet	SS1jet
Trigger	single lepton triggers		single lepton triggers			single & dilepton triggers		
Num. of leptons	4	4	3	3	3	2	2	2
Total lepton charge	0	0	±1	±1	±1	0	±2	±2
Num. of SFOS	2	1	2	1	0	0	0	0
Num. of jets	≤ 1	≤ 1	≤ 1	≤ 1	≤ 1	≥ 2	2	1
Num. of b-tagged jets	0	0	0	0	0	0	0	0
$E_\mathrm{T}^\mathrm{miss}$ [GeV]	> 20	> 20	> 30	> 30	—	> 20	> 50	> 45
$p_\mathrm{T}^\mathrm{miss}$ [GeV]	> 15	> 15	> 20	> 20	—	—	—	—
$\lvert m_{\ell\ell} - m_Z\rvert$ [GeV]	< 10 ($m_{\ell_2\ell_3}$)	< 10 ($m_{\ell_2\ell_3}$)	> 25	> 25	—	—	> 15	> 15
Min. $m_{\ell\ell}$ [GeV]	> 10 ($m_{\ell_0\ell_1}$)	> 10 ($m_{\ell_0\ell_1}$)	> 12	> 12	> 6	> 10	> 12 ($ee,\mu\mu$)	> 12 ($ee,\mu\mu$)
							> 10 ($e\mu$)	> 10 ($e\mu$)
Max. $m_{\ell\ell}$ [GeV]	< 65 ($m_{\ell_0\ell_1}$)	< 65 ($m_{\ell_0\ell_1}$)	< 200	< 200	< 200	< 50	—	—
$m_{4\ell}$ [GeV]	> 140	—	—	—	—	—	—	—
$p_{\mathrm{T},4\ell}$ [GeV]	> 30	—	—	—	—	—	—	—
$M_{\tau\tau}$ [GeV]	—	—	—	—	—	< 66.2	—	—
$\Delta R_{\ell_0\ell_1}$	—	—	< 2.0	< 2.0	—	—	—	—
$\Delta\phi_{\ell_0\ell_1}$ [rad]	< 2.5 ($\Delta\phi_{\ell_0\ell_1}^\mathrm{boost}$)	< 2.5 ($\Delta\phi_{\ell_0\ell_1}^\mathrm{boost}$)	—	—	—	< 1.8	—	—
m_T [GeV]	—	—	—	—	—	< 125	—	> 105 ($m_\mathrm{T}^\mathrm{Lead}$)
Min. $m_{\ell_1 j(j)}$ [GeV]	—	—	—	—	—	—	< 115	< 70
Min. $\phi_{\ell_1 j}$ [rad]	—	—	—	—	—	—	< 1.5	< 1.5
ΔY_{jj}	—	—	—	—	—	< 1.2	—	—
$\lvert m_{jj} - 85\rvert$ [GeV]	—	—	—	—	—	< 15	—	—

Table 2: Definition of each signal region in this analysis. $m_\mathrm{T}^\mathrm{Lead}$ is defined as the transverse mass of the leading lepton and the $\mathbf{E}_\mathrm{T}^\mathrm{miss}$.

dilepton triggers are also used. The p_T thresholds of selected triggers are lower than the cuts applied to offline objects. Single-lepton trigger efficiencies are measured with respect to offline reconstructed leptons using leptonic Z decays. The measured values are approximately 95% for electrons and 90% (70%) for muons in the endcap (barrel).

A specific number of leptons with $p_\mathrm{T} > 15$ GeV is required in each channel of this analysis and the event is discarded if the number of leptons is not equal to the required number. A similar requirement is applied on the number of jets: if the number of jets that satisfy the selection criteria defined in section 5.1 is not equal to the required number, the event is discarded.

5.2.1 Four-lepton channel

Events in this channel are required to have exactly four leptons. The p_T of the leading and sub-leading leptons must be above 25 GeV and 20 GeV, respectively, and the p_T of each of the remaining two leptons must exceed 15 GeV. The total charge of the four leptons is required to be zero. Only events with at least one SFOS lepton pairs are accepted, and events are classified into the signal regions 4ℓ-2SFOS and 4ℓ-1SFOS according to the number of such pairs.

In order to select final states with neutrinos, $E_\mathrm{T}^\mathrm{miss}$ is required to be above 20 GeV and $p_\mathrm{T}^\mathrm{miss}$ above 15 GeV. In order to reduce the $t\bar{t}Z$ background, events are vetoed if they contain more than one jet. Top-quark production is further suppressed by vetoing events with any b-tagged jet with p_T above 20 GeV. The invariant mass of ℓ_2 and ℓ_3, $m_{\ell_2\ell_3}$, is required to satisfy $\lvert m_{\ell_2\ell_3} - m_Z\rvert < 10$ GeV and the invariant mass of ℓ_0 and ℓ_1, $m_{\ell_0\ell_1}$, is required to be between 10 GeV and 65 GeV. This requirement on $m_{\ell_0\ell_1}$ greatly reduces the contamination from $ZZ^{(*)}$ production in events with two pairs of SFOS leptons.

The sensitivity of the search is improved by exploiting two additional variables, $\Delta\phi_{\ell_0\ell_1}^\mathrm{boost}$ and $p_\mathrm{T4\ell}$, where $\Delta\phi_{\ell_0\ell_1}^\mathrm{boost}$ denotes the difference in azimuthal angle between the two leptons from the Higgs boson candidate in the frame where the Higgs boson's p_T is zero. The Higgs boson transverse momentum is approximated with $\vec{p}_\mathrm{T}^H \sim -\vec{p}_\mathrm{T}^Z - \vec{p}_\mathrm{T}^\mathrm{jet}$, or with $\vec{p}_\mathrm{T}^H \sim -\vec{p}_\mathrm{T}^Z$ if no jet is present. The angular separation $\Delta\phi_{\ell_0\ell_1}^\mathrm{boost}$

is requested to be below 2.5 rad. The magnitude of the vector sum of the lepton four-momenta, $p_{T4\ell}$, can discriminate against the main background, $ZZ^{(*)}$, which has no neutrinos. A cut requiring $p_{T4\ell} > 30$ GeV is introduced for 4ℓ-2SFOS. In this signal region the invariant mass of the four leptons is required to be above 140 GeV to remove events from $H \rightarrow ZZ^* \rightarrow 4\ell$, which are the target of another analysis [17].

5.2.2 Three-lepton channel

For this channel, exactly three leptons are required, which must have $p_T > 15$ GeV and correspond to a total charge ± 1. After this requirement, contributions from background processes that include more than one fake lepton, such as single W+jet production and inclusive $b\bar{b}$ pair production, are negligible. Events are then split into the signal regions 3ℓ-2SFOS, 3ℓ-1SFOS and 3ℓ-0SFOS, requiring two, one and zero SFOS lepton pairs, respectively.

In order to reduce the background from $t\bar{t}$ production, events are vetoed if they contain more than one jet. The background from top-quark production is further suppressed by vetoing events if they contain any b-tagged jet with $p_T > 20$ GeV and $|\eta| < 2.5$. In order to select final states with neutrinos, E_T^{miss} is required to be above 30 GeV and p_T^{miss} above 20 GeV in 3ℓ-2SFOS and 3ℓ-1SFOS. In the 3ℓ-0SFOS, E_T^{miss} selections are not imposed because the main backgrounds also contain neutrinos. The invariant mass of all SFOS pairs in 3ℓ-2SFOS and 3ℓ-1SFOS is required to satisfy $|m_{\ell\ell} - m_Z| > 25$ GeV. This requirement suppresses the WZ and ZZ^* backgrounds and reduces the Z+jets acceptance.

A lower threshold is set on the smallest invariant mass of opposite-sign leptons at 12 GeV in 3ℓ-2SFOS and 3ℓ-1SFOS and at 6 GeV in 3ℓ-0SFOS. In addition, an upper threshold is set on the largest invariant mass of opposite-sign leptons at 200 GeV in the three signal regions. These selections reject backgrounds from heavy flavour and reduce the number of combinatorial lepton pairs from the $WZ/W\gamma^*$ process. The $WZ/W\gamma^*$ process could indeed give larger mass values with respect to the WH process since it can proceed through the t- and u-channels, in addition to the s-channel which is present also in WH production. .

The angular separation in ΔR between ℓ_0 and ℓ_1, $\Delta R_{\ell_0\ell_1}$, is required to be smaller than 2 in 3ℓ-2SFOS and 3ℓ-1SFOS. This cut favours the Higgs boson decay topology with respect to that of $WZ/W\gamma^*$ events.

In 3ℓ-2SFOS and 3ℓ-1SFOS, the shape of a multivariate discriminant based on a Gradient Boosted Decision Tree (BDT) [62], which produces a multivariate classifier (BDT Score), is used to achieve a further separation between signal and background. The main purpose of the multivariate classifier is to distinguish between the signal and the dominant $WZ/W\gamma^*$ and ZZ^* backgrounds, and the BDT is trained against these two background processes. The BDT parameters have been tuned in order to ensure that there is no overtraining, i.e. that the BDT is robust against statistical fluctuations in the training samples. For the training of the BDT the input discriminating variables which provide the best separation between signal and background are: the p_T of the three leptons, the magnitude of their vector sum, the invariant mass of the two opposite sign lepton pairs, $\Delta R_{\ell_0\ell_1}$, E_T^{miss}, and p_T^{miss}. In the final likelihood fit, the shape of the distribution of the BDT Score is used to extract the number of observed events in 3ℓ-2SFOS and 3ℓ-1SFOS, while the shape of the distribution of $\Delta R_{\ell_0\ell_1}$ is used to extract the number of observed events in 3ℓ-0SFOS.

5.2.3 Opposite-sign two-lepton channel

In the channel with two leptons of different-flavour and opposite-sign (2ℓ-DFOS), exactly two leptons with p_T thresholds of 22 and 15 GeV are required. Only opposite-sign $e\mu$ final states are considered in order to reduce the background from Z+jets, WZ and ZZ production. A cut on the invariant mass of the lepton pair, $m_{\ell\ell} > 10$ GeV, is applied to reject combinatorial dilepton backgrounds. In order to select final states with neutrinos, E_T^{miss} is required to be above 20 GeV. These selections reduce the background processes that contain jets faking leptons. The presence of at least two jets with $p_T > 25$ GeV is required.

The background from top-quark production is further reduced by vetoing events if they contain any b-tagged jets. To reject the Z+jets production that leads to $e\mu$ final states through $Z \rightarrow \tau\tau$ decay, a cut $M_{\tau\tau} < |m_Z - 25\text{ GeV}|$ is applied, where $M_{\tau\tau}$ is the dilepton invariant mass reconstructed under assumptions that the lepton pair comes from τ lepton decay, the neutrinos are the only source of $E_{\mathrm{T}}^{\mathrm{miss}}$ and neutrinos are collinear to charged leptons [22].

Upper bounds on the invariant mass of the lepton pair, $m_{\ell\ell} < 50$ GeV, and on the azimuthal angular separation of the lepton pair, $\Delta\phi_{\ell\ell} < 1.8$ rad, are applied to enhance the Higgs boson signal relative to the WW, top and W+jets backgrounds. A cut on the rapidity separation between the two jets with leading p_{T}, $\Delta Y_{jj} < 1.2$, and one on the invariant mass of the leading two jets, $|m_{jj} - 85\;\text{GeV}| < 15$ GeV, are required to select jets from the associated W/Z bosons. The central value of the m_{jj} selection interval is larger than the W boson mass in order to retain the acceptance for the ZH production with $Z \rightarrow jj$ decay. The selection $m_{\mathrm{T}} < 125$ GeV is applied, where m_{T} is the transverse mass of the dilepton system defined as $m_{\mathrm{T}} = \sqrt{(E_{\mathrm{T}}^{\ell\ell} + E_{\mathrm{T}}^{\mathrm{miss}})^2 - |\mathbf{p_{\mathrm{T}}}^{\ell\ell} + \mathbf{E_{\mathrm{T}}}^{\mathrm{miss}}|^2}$, where $E_{\mathrm{T}}^{\ell\ell} = \sqrt{|\mathbf{p_{\mathrm{T}}}^{\ell\ell}|^2 + m_{\ell\ell}^2}$.

5.2.4 Same-sign two-lepton channel

Exactly two leptons with the same charge are required for this channel. The lepton p_{T} thresholds are set at 22 and 15 GeV and both same-flavour and different-flavour combinations are considered. A lower bound on $m_{\ell\ell}$ is applied at 12 GeV for same-flavour lepton pairs and at 10 GeV for different-flavour lepton pairs. Despite the same-charge requirement, a wrong-charge assignment may allow background contributions from Z boson decays. Therefore a veto on same-flavour lepton pairs with $|m_{\ell\ell} - m_Z| < 15$ GeV is introduced.

The signal regions 2ℓ-SS2jet and 2ℓ-SS1jet are defined requiring the number of jets to be exactly two or exactly one, respectively. Events with b-tagged jets having $p_{\mathrm{T}} > 20$ GeV are removed in both 2ℓ-SS2jet and 2ℓ-SS1jet. $E_{\mathrm{T}}^{\mathrm{miss}}$ is required to be larger than 50 GeV in 2ℓ-SS2jet and larger than 45 GeV in 2ℓ-SS1jet. Additional cuts are applied to events in 2ℓ-SS2jet and 2ℓ-SS1jet, on the following variables: the minimum invariant mass of a lepton and the jet (the two jets) in the event, $m_{\ell\mathrm{j}}^{\mathrm{min}}(m_{\ell\mathrm{jj}}^{\mathrm{min}})$; the smallest opening angle between the lepton which minimises the above variable and a jet, $\Delta\phi_{\ell\mathrm{j}}^{\mathrm{min}}$; the transverse mass of the leading lepton and the $\mathbf{E_{\mathrm{T}}}^{\mathrm{miss}}$, $m_{\mathrm{T}}^{\mathrm{Lead}}$ (see Table 5.2 for details). Low values of $m_{\ell\mathrm{j}}^{\mathrm{min}}(m_{\ell\mathrm{jj}}^{\mathrm{min}})$ and of $\Delta\phi_{\ell\mathrm{j}}^{\mathrm{min}}$ favour the selection of Higgs decays products with respect to the major backgrounds. High values of $m_{\mathrm{T}}^{\mathrm{Lead}}$ help in reducing the W+jets background. The p_{T} threshold for the sub-leading muon in the $\mu\mu$ channel is increased to 20 GeV in both 2ℓ-SS2jet and 2ℓ-SS1jet to suppress fake muons from W+jets and multijet production processes.

In the fit explained in section 9, 2ℓ-SS2jet and 2ℓ-SS1jet are further split into four signal regions according to the combination of lepton flavours in each event: ee, $e\mu$, μe and $\mu\mu$, where $e\mu$ refers to the case in which electron has leading p_{T} while μe refers to the case in which muon has leading p_{T}. This splitting is motivated by the expected differences in the background contribution such as of $W\gamma$.

5.2.5 Signal acceptance

The number of expected $V(H \rightarrow WW^*)$ events surviving the event selections described for each channel is presented in Table 5.2.5. The total acceptance for $W(H \rightarrow \ell\nu\ell\nu)$, for $W(H \rightarrow \ell\nu qq)$ and for $Z(H \rightarrow \ell\nu\ell\nu)$ is 3.7%, 0.3% and 1.9%, respectively. The analysis acceptance for the ZH with $H \rightarrow \ell\nu qq$ process is negligible. The acceptance is defined as the ratio of the number of events in the SRs to the number of events expected according to the branching ratio for the various processes. The Higgs boson associated production followed by the decay $H \rightarrow \tau\tau$ cannot be completely isolated from the selected final states. Therefore statistical results will be presented considering this component as part of the background, with $\sigma_{\mathrm{VH}} \cdot \mathrm{Br}(H \rightarrow \tau\tau)$ fixed to the SM values.

(a) 8 TeV data analysis

Channel	4ℓ		3ℓ			2ℓ		
Category	2SFOS	1SFOS	2SFOS	1SFOS	0SFOS	DFOS	SS2jet	SS1jet
WH ($H \to WW^*$)	—	—	0.563	1.43	1.284	1.48	1.02	1.84
ZH ($H \to WW^*$)	0.208	0.235	0.168	0.179	0.145	0.668	0.017	0.195
VH ($H \to WW^*$)	0.208	0.235	0.731	1.62	1.428	2.15	1.04	2.04
(all categories)	9.44							

(b) 7 TeV data analysis

	2SFOS	1SFOS	2SFOS	1SFOS	0SFOS	DFOS
WH ($H \to WW^*$)	—	–	0.116	0.292	0.263	0.210
ZH ($H \to WW^*$)	0.023	0.021	0.013	0.033	0.028	0.075
VH ($H \to WW^*$)	0.023	0.021	0.129	0.325	0.291	0.285
(all categories)	1.073					

Table 3: Number of expected signal events, for $m_H = 125$ GeV, in the (a) 8 TeV and (b) 7 TeV data samples.

6 Background Modelling

The background contamination in the signal regions results from various physics processes, each modelled by one of the following methods:

- Pure MC prediction: rates and shapes are extracted from simulation and normalized to the values in Table 1;

- MC prediction normalised to data: rates are extracted from data in a control region (CR) but shapes are extracted from MC;

- Pure data-driven prediction: rates and shapes are extracted from data.

Fake-lepton backgrounds (W+jets, Multijets) in the 2ℓ channels are estimated by using a purely data-driven method which utilises the rate at which a jet fakes a lepton. Details of this method can be found in Ref. [22]. Table 6 summarises the method adopted for each process in each signal region. The labels 'MC' and 'Data' represent the pure MC prediction and the pure data-driven estimation. For backgrounds that are modelled by MC with a normalisation factor computed using data, the CR name is shown as defined in Table 6 and 6. In the table 'VVV' represents the triboson processes WWW^*, ZWW^*, ZZZ^* and $WW\gamma^*$. The 'Top' processes include $t\bar{t}$ and single top production, the latter dominated by tW with $W \to \ell\nu$ decay, as well as $t\bar{t}W/Z$. The ratio of $t\bar{t}$ yields to tW yields is found compatible between all the CRs and associated SRs, thus only one normalisation factor (NF) is extracted per CR for the 'Top' category. In this analysis Higgs boson production through ggF and VBF is treated as background as discussed in section 9.

	4ℓ	3ℓ	2ℓ	
Category	2SFOS, 1SFOS	2SFOS, 1SFOS, 0SFOS	DFOS	SS2jet, SS1jet
Process				
VVV	MC	MC	MC	MC
$WZ/W\gamma^*$	—	3ℓ-CR-WZ, 3ℓ-CR-Zjets	MC	2ℓ-CR-WZ
ZZ^*	4ℓ-CR-ZZ	3ℓ-CR-ZZ, 3ℓ-CR-Zjets	MC	MC
OS WW	—	MC	MC	2ℓ-CR-WW
SS WW	—	MC	—	MC
$W\gamma$	—	—	—	2ℓ-CR-Wgamma
$Z\gamma$	—	3ℓ-CR-Zgamma	MC	MC
Z/γ^*	—	3ℓ-CR-Zjets, 3ℓ-CR-ZZ	2ℓ-CR-Ztautau	2ℓ-CR-Zjets
W+jets	—	—	Data	Data
Multijets	—	—	Data	Data
Top	MC	3ℓ-CR-Top	2ℓ-CR-OSTop	2ℓ-CR-SSTop

Table 4: Summary of background modelling. Some backgrounds are normalised rescaling the MC yields by the data to MC ratio measured in CRs. For these backgrounds the names of the most important CRs are listed. The symbol '—' means that the contribution to the total background in the signal region is negligible.

The CRs used in the 4ℓ and 3ℓ analyses are defined in Table 6 and those used in the 2ℓ analyses are shown in Table 6. The CRs are orthogonal to the corresponding SRs by inverting some cuts with respect to the SR definitions. These cuts are in boldface fonts in the tables and are further explained in the following sections.

Channel	4ℓ	3ℓ				
CR	CR-ZZ	CR-WZ	CR-ZZ	CR-Zjets	CR-Top	CR-Zgamma
Number of leptons	4	3	3	3	3	3
Total lepton charge	0	±1	±1	±1	±1	±1
Number of SFOS	2	2 or 1	2 or 1	2 or 1	2 or 1	2 or 1
		($ee\mu$ or $\mu\mu\mu$)				($\mu\mu e$ or eee)
Number of jets	≤ 1	≤ 1	≤ 1	≤ 1	≥ 1	≤ 1
Number of b-tagged jets	0	0	0	0	$\geq \mathbf{1}$	0
$E_{\mathrm{T}}^{\mathrm{miss}}$ (and/or) $p_{\mathrm{T}}^{\mathrm{miss}}$ [GeV]	—	> 30 and > 20	**< 30 or < 20**	**< 30 and < 20**	> 30 and > 20	**< 30 or < 20**
$|m_{\ell\ell} - m_Z|$ [GeV]	$< 10(m_{\ell_2\ell_3})$	**< 25**	—	**< 25**	> 25	—
$|m_{\ell\ell\ell} - m_Z|$ [GeV]	—	—	< 15	> 15	—	**< 15**
Min. $m_{\ell\ell}$ [GeV]	$> \mathbf{65(m_{\ell_0\ell_1})}$	> 12	> 12	> 12	> 12	> 12
Max. $m_{\ell\ell}$ [GeV]	—	< 200	< 200	< 200	—	< 200
$\Delta R_{\ell_0\ell_1}$	—	< 2.0	< 2.0	< 2.0	—	< 2.0

Table 5: Control region definitions in 4ℓ and 3ℓ analyses. Cuts indicated in boldface fonts are designed to keep the CR orthogonal to the relevant SR.

Channel	DFOS 2ℓ		SS 2ℓ				
CR	CR-OSTop	CR-Ztautau	CR-Wgamma	CR-WZ	CR-WW	CR-SSTop	CR-Zjets
Number of leptons	2	2	2 **≥ 1 conversion e**	**3**	2	2	2
Total lepton charge	0	0	±2	±1	**0**	**0**	**0**
Number of SFOS	0	0	—	—	—	—	—
Number of jets	≥ 2	≥ 2	2 or 1	2 or 1	2 or 1	2 or 1	2 or 1
Number of b-tagged jets	0	0	0	0	0	$\geq \mathbf{1}$	0
$E_{\mathrm{T}}^{\mathrm{miss}}$ [GeV]	> 20	> 20	> 45 (1j) > 50 (2j)	> 45 (1j) > 50 (2j)	> 85 (1j) > 80 (2j)	> 45 (1j,$ee,\mu\mu$) > 60 (1j,$e\mu$) > 50 (2j,$ee,\mu\mu$) > 60 (2j,$e\mu$)	> 45 (1j) < 85 (1j,$e\mu$) > 50 (2j,$ee,\mu\mu$) < 80 (2j,$e\mu$)
$|m_{\ell\ell} - m_Z|$ [GeV]	—	—	—	< 15($OS\ ee,\mu\mu$)	> 15($ee,\mu\mu$)	> 15($ee,\mu\mu$)	**< 15**($ee,\mu\mu$)
Min. $m_{\ell\ell}$ [GeV]	> **90 (8** TeV) > **80 (7** TeV)	> 10	> 12($ee,\mu\mu$) > 10($e\mu$)	> 12($ee,\mu\mu$) > 10($e\mu$)	> 12($ee,\mu\mu$) > 10($e\mu$)	> 12($ee,\mu\mu$) > 12($e\mu$)	> 12($ee,\mu\mu$) > 55($e\mu$)
Max. $m_{\ell\ell}$ [GeV]	—	< 70	< 50	—	—	—	< 80($e\mu$)
$M_{\tau\tau}$ [GeV]	< ($m_Z - 25$)	—	—	—	—	—	—
$\Delta\phi_{\ell_0\ell_1}$ [rad]	—	> **2.8**	< 2.5	—	—	—	—
m_{T} [GeV]	—	—	> 105 (1j)	> 105 (1j)	> 105 (1j)	> 105 (1j)	—
Min. $m_{\ell_1 j}$ [GeV]	—	—	< 70	< 70	< 70	< 70	< 70
Min. $m_{\ell_1 jj}$ [GeV]	—	—	< 115	< 115	< 115	< 115	< 115
Min. $\phi_{\ell_1 j}$ [rad]	—	—	< 1.5	< 1.5	—	—	—
$p_{\mathrm{T}}^{\ell\ell}$ [GeV]	—	—	> 30	—	—	—	—

Table 6: Control region definitions in 2ℓ analyses. Cuts indicated in boldface fonts are designed to keep the CR orthogonal to the relevant SR.

6.1 Background in four-lepton channel

The main backgrounds that contribute to the 4ℓ-2SFOS and 4ℓ-1SFOS signal regions are diboson processes, dominated by ZZ^* production with $E_{\mathrm{T}}^{\mathrm{miss}}$ from $Z \rightarrow \tau\tau$ decay, and three vector boson processes, in particular ZWW^* which has the same signature as the signal. These processes respectively account for about 85% and 15% of the total background contamination. To normalise the ZZ^* background a dedicated CR, the 4ℓ-CR-ZZ control region, is defined by inverting the cut on the invariant mass of dileptons from the Higgs boson candidate. All the other minor background processes, listed in Table 6, are modelled by simulation.

6.2 Background in the three-lepton channel

Three classes of backgrounds contribute to the 3ℓ analysis. Firstly, diboson processes: $WZ/W\gamma^*$, ZZ^*, with an undetected lepton mainly due to its low-p_{T}, and $Z\gamma$, in which the photon converts to electron-

positron pairs. Note that ZZ^* contribution in this channel is due to single resonant ZZ^* production where the three-lepton invariant mass is just below the Z boson mass. The second class includes triboson processes, mainly WWW^*. The last class of backgrounds are processes with a fake lepton from a jet, mainly Z+jets and top-quark production processes.

In the 3ℓ-2SFOS and 3ℓ-1SFOS signal regions, $WZ/W\gamma^*$ and ZZ^* represent the leading background contributions accounting for about 80% of total background yields, with 65% from $WZ/W\gamma^*$ and 15% from ZZ^*. Production of $Z\gamma$, VVV, Z+jets and top-quark equally share the remaining background fraction. The 3ℓ-0SFOS region contains similarly-sized contributions from $WZ/W\gamma^*$, VVV and top-quark production. In this category the total background is about eight times lower than in 3ℓ-2SFOS and 3ℓ-1SFOS.

A 3ℓ-CR-WZ control region is defined by reversing the Z-veto cut, in order to select events with Z boson decays. The 3ℓ-CR-ZZ and 3ℓ-CR-Zgamma control regions are defined by requiring low E_T^{miss} values to reflect the absence of final-state neutrinos in the background process under study. For these CR, the invariant mass of the three leptons must be consistent with the Z boson mass. These regions are further distinguished according to the flavour combination of the three leptons, namely eee or $\mu\mu e$ for the 3ℓ-CR-Zgamma control region, and $\mu\mu\mu$ or $ee\mu$ for the 3ℓ-CR-ZZ control region.

The 3ℓ-CR-Zjets control region is defined by reversing the E_T^{miss} cuts and the Z-veto cut. The properties of jets misidentified as leptons are different for fake electrons and fake muons, therefore the 3ℓ-CR-Zjets control region is further split into separate regions for the electron fake component ($eee + \mu\mu e$ events) and for the muon fake component ($\mu\mu\mu + ee\mu$ events) and a NF is assigned to each component. In the 7 TeV analysis the statistics in the 3ℓ-CR-Zjets control region with the lepton flavour combination of $\mu\mu\mu$ or $ee\mu$ is too small to reliably extract the NF and the estimation of the fake muon component is taken directly from MC.

The 3ℓ-CR-Top control region is defined by requiring at least one b-tagged jet. The Z+jets process is difficult to isolate from other processes that include Z bosons in their final state, thus the NF for this process is constrained not only by the 3ℓ-CR-Zjets control region, but also in part by the 3ℓ-CR-WZ and the 3ℓ-CR-ZZ ones, as indicated in Table 6.

6.3 Background in the opposite-sign two-lepton channel

The dominant background in this channel is from top-quark production, which accounts for about 50% of the total contamination. The 2ℓ-CR-OSTop control region is defined by requiring a high invariant mass of the lepton pair in the final state. As the b-jet rejection criteria are the same in the CR and in the SR, the systematic uncertainties related to b-tagging largely cancel between the 2ℓ-CR-OSTop control region and the 2ℓ-DFOS signal region. The second dominant background is $Z \to \tau\tau$, which accounts for 20% of the total background in the SR. A dedicated control region, 2ℓ-CR-Ztautau, is defined by requiring a large opening angle between the two leptons. The WW process constitutes the third largest background accounting for 10% of the total. Due to the difficult separation of this process from $t\bar{t}$ events over a wide kinematic region, no dedicated CR is defined, and this process is modelled solely by MC.

The contribution of backgrounds with fake leptons from jets, W+jets and multijet, accounts for 10% of the total background. The fake-lepton background rate is affected by a 40% uncertainty. Due to this large uncertainty, backgrounds with fake leptons contribute significantly to the total uncertainty on the expected signal region yield. $WZ/W\gamma^*$ and ggF Higgs boson production, each representing 5% of the total background, are modelled with MC.

6.4 Background in the same-sign two-lepton channel

The two largest backgrounds in this channel are from WZ and W+jets processes, which each accounts for one third of the total background. The $WZ/W\gamma^*$ events with three final leptons enter the selection

when one of them escapes detection. To normalise this process, the 2ℓ-CR-WZ control region is defined by selecting events with three leptons. The contamination from W+jets events with one fake lepton is estimated by using the same data-driven method used in DFOS 2ℓ channel.

The remaining background processes contribute at the 10% level or less. The normalisation of $W\gamma$ production is based on the 2ℓ-CR-Wgamma control region, defined by requiring at least one electron consistent with a conversion, including a requirement that the electron does not have a hit in the innermost pixel layer. Top-quark production, opposite-sign WW and Z+jets contribute to this SR with electrons whose charge is mis-reconstructed. The 2ℓ-CR-SSTop, 2ℓ-CR-WW and 2ℓ-CR-Zjets control regions are defined selecting opposite-sign leptons to normalise these contributions. Moreover, in 2ℓ-CR-SSTop at least one b-tagged jets is selected. Due to the small production rate, no control region is defined to normalise the same-sign WW production from vector boson scattering, whose rate is taken directly from simulation.

6.5 Normalisation factors and composition of control regions

When relevant, the factors used to normalise background processes are extracted from a simultaneous fit to all control and signal regions, further explained in section 9.

Table 6 lists the main background processes, along with the CRs that contribute to the determination of their NF. The NFs, that are specific to each signal region, are fitted taking into account only the total number of expected and observed events in each CR, separately for the 7 TeV and 8 TeV data samples, and are summarised in Table 6.5. The number of events observed and expected from simulation in the 7 TeV and 8 TeV data analysis are summarised in Table 6.5.

Background spectra and the expected composition of the CRs in 8 TeV collisions are shown in Figures 2 to 5.

In these tables and figures, each background process normalised using CRs is presented separately, while backgrounds that are not normalised using CRs are grouped together as 'Others'. In this section the Higgs boson production through ggF and VBF mechanisms and the VH production are included in the 'Others' category, assuming the SM value for the cross sections and a mass of 125 GeV.
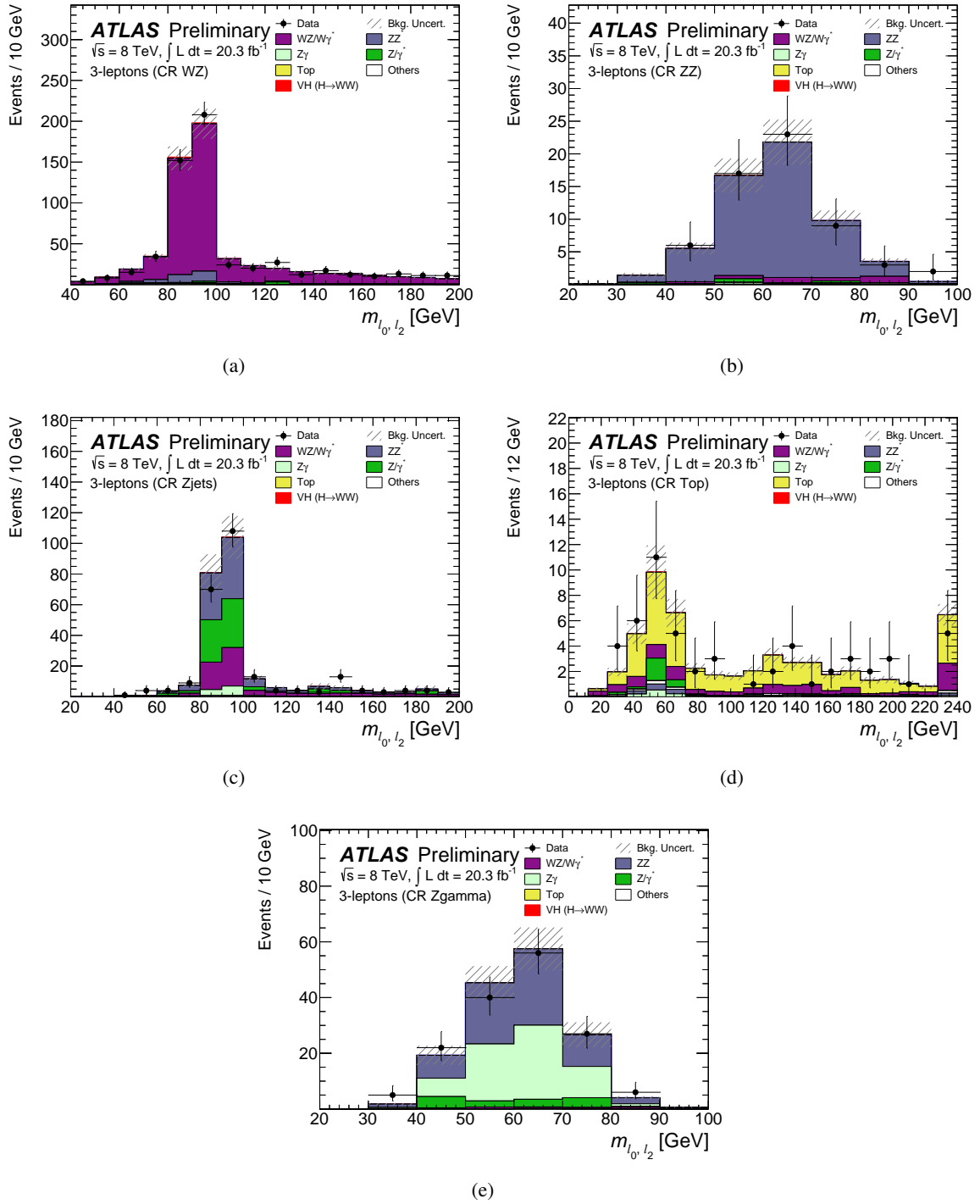
Figure 2: The invariant mass of the two opposite-sign leptons with larger ΔR distance, $m_{\ell_0\ell_2}$, in the five CRs defined in 3ℓ analysis: (a) 3ℓ-CR-WZ, (b) 3ℓ-CR-ZZ, (c) 3ℓ-CR-Zjets, (d) 3ℓ-CR-Top and (e) 3ℓ-CR-Zgamma. Data (dots) are compared to the background expectation (stacked filled histograms), where the background contributions are normalised by applying the NFs derived from the final fit. The hatched area on the histogram represents total uncertainty, both statistical and systematic (see section 7), on the total background estimate. The last bin includes overflow events.
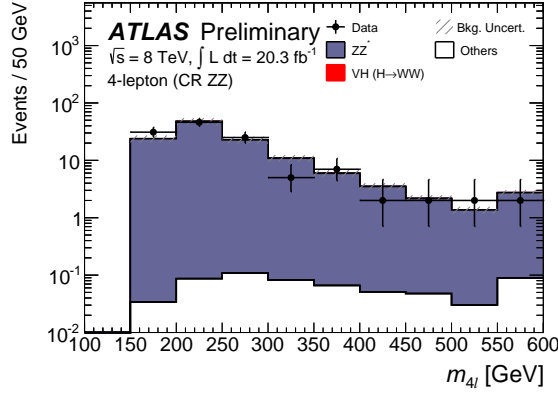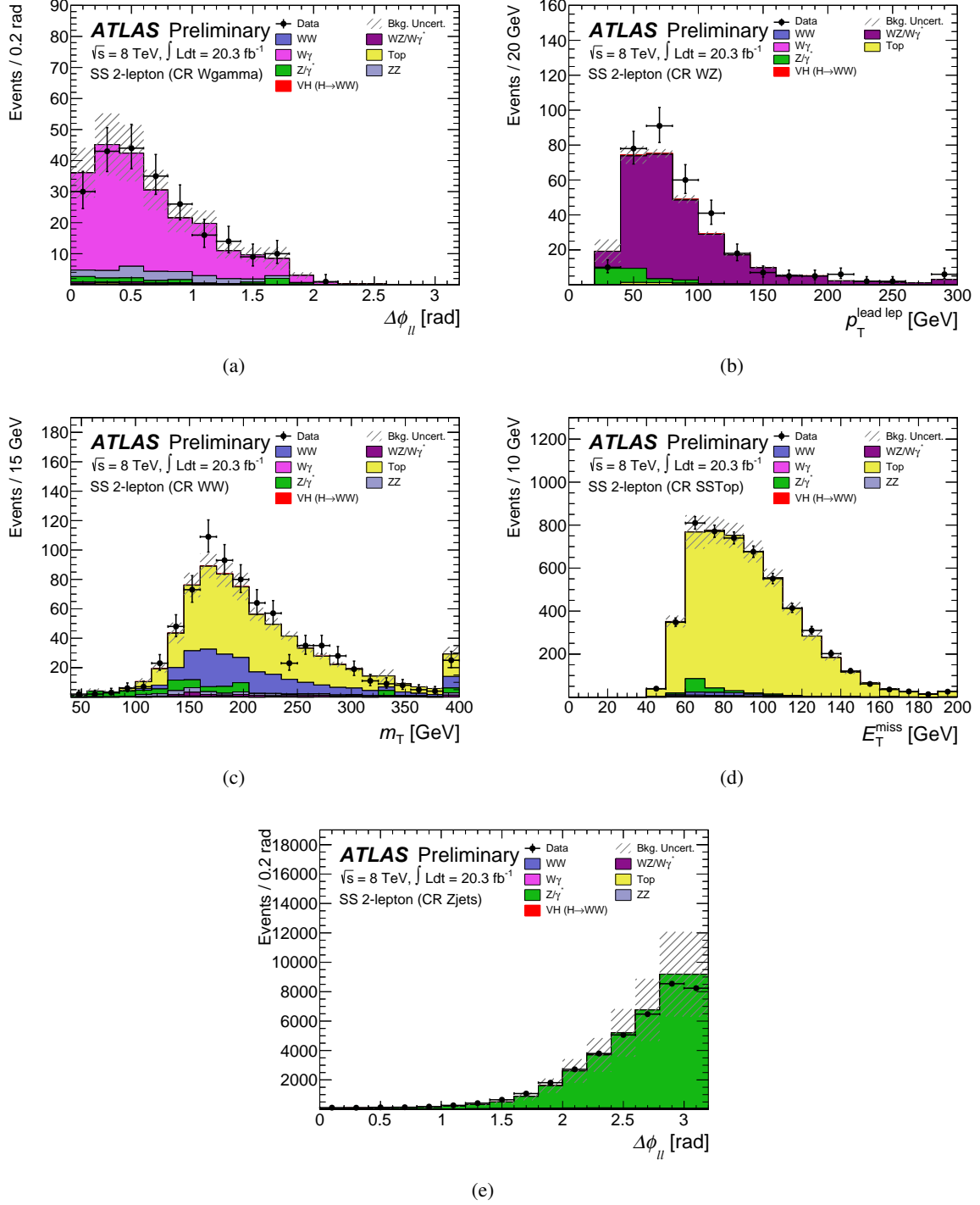
(a)

Figure 3: The invariant mass of the four leptons, $m_{4\ell}$, in the 4ℓ-CR-ZZ control region. Data (dots) are compared to the background expectation (stacked filled histograms), where ZZ^* events are normalised by the NF from the final fit. The hatched area on the histogram represents total uncertainty, both statistical and systematic (see section 7), on the total background estimate. The last bin includes overflow events.
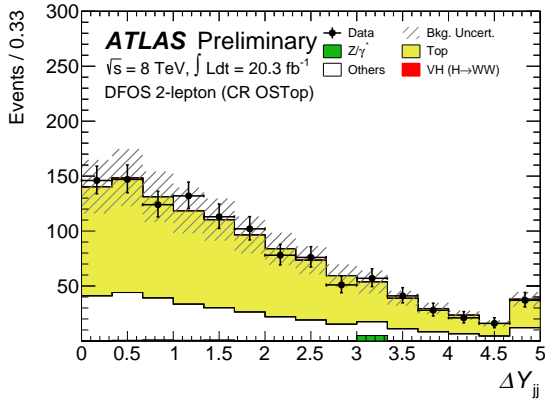
(a)
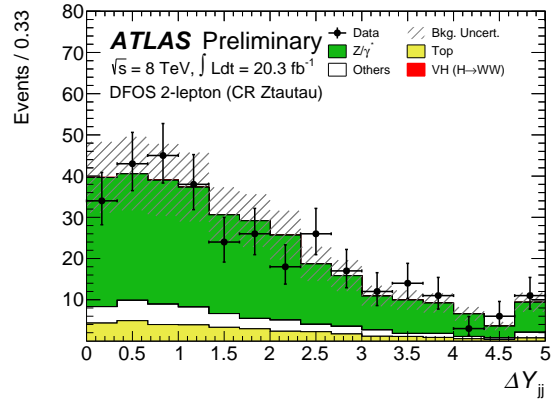
(b)

Figure 4: The rapidity difference between the two jets, ΔY_{jj}, (a) in the 2ℓ-CR-OSTop control region and (b) in the 2ℓ-CR-Ztautau control region. Data (dots) are compared to the background expectation (stacked filled histograms), where the background contributions are normalised by applying the NFs derived from the final fit. The hatched area on the histogram represents total uncertainty, both statistical and systematic (see section 7), on the total background estimate. The last bin includes overflow events.

17

Figure 5: Distribution of relevant variables in the SS 2ℓ analysis control regions: (a) azimuthal angle between the two leptons, $\Delta\phi_{\ell\ell}$, in the Wgamma CR, (b) transverse momentum of the leading lepton, $p_T^{\text{lead lep}}$, in the WZ CR, (c) transverse mass, m_T, in the WW CR, (d) E_T^{miss} in the Top CR and (e) difference in azimuthal angle between the two leptons, $\Delta\phi_{\ell\ell}$, in the Zjets CR. Data (dots) are compared to the background expectation (stacked filled histograms), where the background contributions are normalised by applying the NFs derived from the final fit. The hatched area on the histogram represents total uncertainty, both statistical and systematic (see section 7), on the total background estimate. The last bin includes overflow events.

(a) 8 TeV data analysis

Channel	4ℓ	3ℓ		2ℓ
Category	2SFOS, 1SFOS	2SFOS, 1SFOS, 0SFOS	DFOS	SS2jet, SS1jet
Process				
$WZ/W\gamma^*$	—	$1.08^{+0.08}_{-0.06}$	—	0.94 ± 0.10
ZZ^*	$1.03^{+0.11}_{-0.10}$	$1.28^{+0.22}_{-0.20}$	—	—
OS WW	—	—	—	0.80 ± 0.33
$W\gamma$	—	—	—	1.06 ± 0.12
$Z\gamma$	—	$0.62^{+0.15}_{-0.14}$	—	—
Z/γ^*	—	$0.80^{+0.68}_{-0.53}$ (μ-fake) $0.33^{+0.12}_{-0.11}$ (e-fake)	$0.90^{+0.18}_{-0.16}$	0.86 ± 0.30
Top	—	$1.36^{+0.34}_{-0.30}$	$1.05^{+0.16}_{-0.14}$	1.04 ± 0.08

(b) 7 TeV data analysis

Process				
$WZ/W\gamma^*$	—	$1.02^{+0.12}_{-0.11}$	—	
ZZ^*	$1.59^{+0.36}_{-0.31}$	$1.78^{+0.51}_{-0.42}$	—	
OS WW	—	—	—	
$W\gamma$	—	—	—	
$Z\gamma$	—	$0.45^{+0.09}_{-0.09}$	—	
Z/γ^*	—	$0.68^{+0.16}_{-0.15}$ (e-fake)	$1.11^{+0.38}_{-0.34}$	
Top	—	$1.25^{+0.66}_{-0.52}$	$0.93^{+0.16}_{-0.14}$	

Table 7: Summary of background normalisation factors in the (a) 8 TeV and (b) 7 TeV data analyses. The uncertainties include both statistical and systematic components (see section 7). '—' means that the background process, when considered, is normalised by MC.

(a) 8 TeV data analysis

Channel	4ℓ	3ℓ					2ℓ	
CR	CR-ZZ	CR-WZ	CR-ZZ	CR-Zjets	CR-Top	CR-Zgamma	CR-Ztautau	CR-OSTop
Observed events	122	578	60	251	55	156	328	1169
MC prediction	121 ± 17	576 ± 63	60 ± 10	249 ± 46	55 ± 12	155 ± 31	326 ± 55	1160 ± 150
MC (no NFs)	117 ± 10	543 ± 50	47.9 ± 3.7	351 ± 40	48.4 ± 6.3	188 ± 17	354 ± 56	1120 ± 140
Composition (%)								
$WZ/W\gamma^*$	—	89.3 ± 1.3	5.5 ± 3.0	25.9 ± 2.8	20.3 ± 5.4	1.7 ± 1.0	—	—
ZZ^*	99.5 ± 0.6	6.7 ± 1.0	90.1 ± 3.8	36.3 ± 2.5	3.6 ± 2.5	46.9 ± 4.0	—	—
$Z\gamma$	—	0.54 ± 0.31	0.6 ± 1.0	5.5 ± 1.4	2.3 ± 2.0	42.7 ± 4.0	—	—
Z+jets	—	1.08 ± 0.43	2.1 ± 1.9	29.1 ± 2.9	5.5 ± 3.1	8.3 ± 2.2	78.2 ± 2.3	0.75 ± 0.25
Top	0.02 ± 0.01	0.66 ± 0.34	0.27 ± 0.67	0.08 ± 0.18	64.0 ± 6.5	0.10 ± 0.30	10.5 ± 1.7	71.3 ± 1.3
Others	0.48 ± 0.63	0.81 ± 0.37	1.1 ± 1.4	0.87 ± 0.59	3.7 ± 2.6	0.34 ± 0.46	11.2 ± 1.7	28.0 ± 1.3
$VH\ (H \to WW^*)$	0.02 ± 0.14	0.93 ± 0.40	0.26 ± 0.66	0.37 ± 0.39	0.52 ± 0.97	0.05 ± 0.18	0.10 ± 0.18	0.21 ± 0.24

Channel	SS 2ℓ				
CR	CR-Wgamma	CR-WZ	CR-WW	CR-SSTop	CR-Zjets
Observed events	228	331	769	5142	39731
MC prediction	229 ± 41	311 ± 66	742 ± 63	5080 ± 350	41000 ± 14000
MC (no NFs)	218 ± 35	335 ± 68	787 ± 58	4930 ± 330	47000 ± 16000
Composition (%)					
$W\gamma$	85.0 ± 2.4	—	0.46 ± 0.25	0.049 ± 0.031	0.0221 ± 0.0074
$WZ/W\gamma^*$	1.02 ± 0.66	86.8 ± 1.9	2.34 ± 0.56	0.200 ± 0.063	0.381 ± 0.031
WW	0.37 ± 0.40	0.029 ± 0.097	23.9 ± 1.6	1.43 ± 0.17	0.572 ± 0.037
Z+jets	4.2 ± 1.3	7.0 ± 1.4	7.01 ± 0.94	2.15 ± 0.20	97.701 ± 0.074
Top	0.68 ± 0.54	1.50 ± 0.69	62.7 ± 1.8	95.50 ± 0.29	0.856 ± 0.046
Others	8.7 ± 1.9	5.2 ± 1.3	3.24 ± 0.65	0.63 ± 0.11	0.441 ± 0.033
$VH\ (H \to WW^*)$	—	0.77 ± 0.50	0.32 ± 0.21	0.036 ± 0.027	0.0077 ± 0.0043

(b) 7 TeV data analysis

Channel	4ℓ	3ℓ					2ℓ	
CR	CR-ZZ	CR-WZ	CR-ZZ	CR-Zjets	CR-Top	CR-Zgamma	CR-Ztautau	CR-OSTop
Observed events	24	101	18	81	9	123	55	137
MC prediction	24.2 ± 8.0	101 ± 16	18.1 ± 4.6	85 ± 19	8.8 ± 3.8	123 ± 26	55 ± 15	137 ± 20
MC (no NFs)	15.2 ± 5.1	98.7 ± 9.5	10.7 ± 0.6	94.4 ± 7.6	8.1 ± 1.4	208 ± 12	51 ± 12	145 ± 18
Composition (%)								
$WZ/W\gamma^*$	—	87.5 ± 3.3	3.1 ± 4.1	11.4 ± 3.4	13.7 ± 11.6	0.6 ± 0.7	—	—
ZZ^*	99.8 ± 1.0	7.4 ± 2.6	92.7 ± 6.1	33.2 ± 5.1	4.2 ± 6.7	31.8 ± 4.2	—	—
$Z\gamma$	—	1.8 ± 1.3	0.6 ± 1.7	38.3 ± 5.3	6.5 ± 8.3	59.2 ± 4.4	—	—
Z+jets	—	1.5 ± 1.2	3.0 ± 4.0	16.8 ± 4.0	0.3 ± 2.0	8.3 ± 2.5	76.0 ± 5.8	0.14 ± 0.32
Top	0.03 ± 0.01	0.70 ± 0.83	—	0.07 ± 0.29	71 ± 15	0.03 ± 0.16	13.3 ± 4.6	75.1 ± 3.7
Others	0.20 ± 0.90	0.59 ± 0.76	0.5 ± 1.6	0.27 ± 0.56	4.2 ± 6.8	0.06 ± 0.22	10.7 ± 4.2	24.8 ± 3.7
$VH\ (H \to WW^*)$	0.02 ± 0.31	0.53 ± 0.72	0.11 ± 0.77	0.03 ± 0.20	0.4 ± 2.1	0.01 ± 0.11	0.05 ± 0.29	0.14 ± 0.31

Table 8: Number of observed and predicted events and background composition in the CRs for the 4ℓ, 3ℓ and 2ℓ topologies in the (a) 8 TeV and (b) 7 TeV data analyses. NFs are taken into account in the calculation of the composition. The uncertainties on event yields include both statistical and systematic components (see section 7), binomial errors are assigned to the percentages.

7 Systematic Uncertainties

The theoretical and experimental sources of systematic uncertainties on the signal and on the total background are described in this section, and summarised in Table 9 (a) for the signal and in Table 9 (b) for the background. In the Tables the final post-fit uncertainties on the estimated yields of 8 TeV data analysis are shown. Similar values are obtained for the 7 TeV data analysis. The uncertainties are grouped in different categories and explained in the following sub-sections.

7.1 Normalisation uncertainties

The theoretical uncertainties on the total Higgs boson production cross section and the Higgs boson branching ratio are evaluated following the recommendation of the LHC Higgs cross section working group [21, 28, 29]. Uncertainties concerning renormalisation and factorisation scales (QCD scales), parton distribution functions (PDF), the value of α_s and branching ratios are estimated. The main uncertainty on the VH signal, shown in the 'NLO Acceptance' row of Table 9, accounts for the variations in the acceptance when NLO effects and different parton showering models are included. It is estimated to be 10% in each SR category by comparing the acceptance of Pythia8 with respect to Powheg+Pythia8 or Powheg+Herwig. Another important uncertainty on the VH and the VBF processes is the one on the Higgs boson branching ratio to WW^* which amounts to 4%. In the row labelled 'Higgs boson branch. fraction' of Table 9 a small contribution to the uncertainty from the $H \rightarrow \tau\tau$ branching ratio is also included. The scale uncertainty is about 1% for WH production. It is larger (3%) for ZH production due to the contribution of the gluon-gluon initiated process. The acceptance of the $gg \rightarrow ZH$ ($H \rightarrow WW^*$) is evaluated as 8% of the $qq \rightarrow ZH$ ($H \rightarrow WW^*$) with a relative uncertainties of 5%. The PDF uncertainties of the $gg \rightarrow ZH$ ($H \rightarrow WW^*$) and the $qq \rightarrow ZH$ ($H \rightarrow WW^*$) are anti-correlated. In the other categories, the acceptances of the $gg \rightarrow ZH$ ($H \rightarrow WW^*$) are estimated as 8 (6.8)% of the $qq \rightarrow ZH$ ($H \rightarrow WW^*$) in 8 (7) TeV data. A relative uncertainty of 100% is assigned to these acceptance estimations. For the ggF process the uncertainties on the production cross section, from the renormalisation and factorisation scales and from the choice of PDFs and α_s, ranging from 7% to 8%, constitute the main contributions. The 'VH NLO EW corrections' of Table 9 refers to additional uncertainties on the corrections [32] to the differential cross section, applied as a function of the Higgs boson p_T on the LO WH and ZH signals generated with Pythia8. The size of this uncertainty is about 2%. A reweighting is also applied to the the Higgs boson p_T spectrum from the ggF process to account for the EW corrections from NLO to NNLO, and the change in the acceptance is evaluated to estimate the related uncertainty. In the opposite-sign 2ℓ channel, an additional uncertainty on the jet bin migration due to the QCD scale on the ggF process is estimated by using a Powheg+MINLO approach [63], to account for mismodelling of secondary jets generated by Powheg. Additional contributions from the $gg \rightarrow ZH$ ($H \rightarrow WW^*$) are taken into account in the statistical interpretation: in the 4ℓ categories using 8 TeV data, in which the process is the most relevant, dedicated MC samples are generated and all the uncertainties are estimated as for the other processes.

The uncertainties from the QCD scales for the main background sources are estimated using mainly MCFM, by varying the scales up and down independently by a factor of two. In the 4ℓ channel the size of the variation on the ZZ^* background from different scales is about 4% in both the SRs and CR, therefore the uncertainty is negligible due to cancellations. In the 3ℓ-2SFOS and 3ℓ-1SFOS category the scale uncertainties on the $WZ/W\gamma^*$ process are determined for each bin of the BDT output and range between 3% and 6%. In the same-sign 2ℓ channel, due to cancellations from the CRs the scale uncertainties on $WZ/W\gamma^*$ and $W\gamma$ backgrounds are found to be negligible with the exception of the 2ℓ-SS2jet in which 100% uncertainty is assigned to the $W\gamma$ process. The scale uncertainty on the same-sign WW+2jet background, estimated using VBF@NLO [64], is of the order of 40%. In the opposite-sign 2ℓ channel, QCD scale uncertainties on top and WW+2jet production with at least two QCD couplings, referred to as

QCD *WW* in the following, are estimated to be about 9% and 17% by using MC@NLO and MADGRAPH, respectively.

The PDF uncertainties are calculated for all the relevant backgrounds by following the PDF4LHC recipe [65], i.e., using the envelope of predictions from MSTW2008, CT10 and NNPDF2.3 PDF sets. In the top background in the opposite-sign 2ℓ channel the PDF uncertainty is evaluated using the same technique used in the ggF-enriched $n_j \geq 2$ category in Ref. [22]. The uncertainties range from 1% to 6%, depending on the nature of the background process and the signal category. An uncertainty of 33% on the K-factor of triboson process is evaluated using VBF@NLO; in the 3ℓ-0SFOS signal region this uncertainty is estimated in bins of $\Delta R_{\ell_0,\ell_1}$ and ranges from 1% to 6%.

The 'MC modelling' row of Table 9 (b) takes into account the yield variation observed between the predictions of different MC generators. In the 3ℓ channel, POWHEG and aMC@NLO are compared to evaluate the modelling uncertainty on $WZ/W\gamma^*$. In the opposite-sign 2ℓ channel, POWHEG+PYTHIA and POWHEG+HERWIG are used for top, MADGRAPH is compared to SHERPA for QCD *WW*, and ALPGEN+PYTHIA and ALPGEN+HERWIG are compared for $Z \rightarrow \tau\tau$. In the same-sign 2ℓ channel, POWHEG+PYTHIA and MC@NLO are compared for *WZ*. SHERPA is compared to POWHEG for ZZ^* in the 4ℓ channel. The 'CR statistics' uncertainties arise from the number of data and simulated events populating the CRs.

7.2 Experimental uncertainties

One of the dominant experimental systematic uncertainties, labelled 'Jet' in Table 9, come from the propagation of the jet energy scale calibration and resolution uncertainties. They were derived from a combination of simulation, test-beam data, and in situ measurements [66]. Additional uncertainties due to differences between quark and gluon jets, and between light and heavy flavour jets, as well as the effect of pileup interactions are included. For jets used in this analysis, the jet energy scale uncertainty ranges from 1% to 7%, depending on p_T and η. The relative uncertainty on the jet energy resolution ranges from 2% to 40%, with the largest value of the resolution and relative uncertainty occurring at the p_T threshold of the jet selection. Jet, electron and muon energy scale uncertainties are propagated to the E_T^{miss} evaluation. An additional 'E_T^{miss} Soft term' uncertainty is associated with the contribution of energy deposits not assigned to any reconstructed objects to the E_T^{miss} reconstruction [59–61]. The 'Muon' and 'Electron' uncertainties include those from lepton reconstruction, identication and isolation, as well as lepton energy and momentum measurements. The 'Trigger efficiency' uncertainty of Table 9 refers to the systematic uncertainty on the lepton trigger efficiencies. The uncertainties on the lepton and trigger effciencies are of the order of 1% or smaller. The 'b–tagging efficiency' row refers to the uncertainties on the efficiency of tagging of b–jets and include contributions from b–jet identification and charm and light-flavour jet rejection factors [58,67]. The uncertainties related to b–jet identification range from <1% to 8%. The uncertainties on the misidentification rate for light-quark jets depend on p_T and η, and have a range of 9-19%. The uncertainties on c–jets reconstructed as b–jets range between 6% and 14% depending on p_T. The uncertainty labelled as 'Fake factor' is associated to the data-driven estimates of the *W*+jets and multijet backgrounds, it ranges between 35% and 45% depending on the sample and on the signal category. A 'Charge mis-assignment' systematic uncertainty is estimated to account for the mismodelling of the charge flip effect by comparing the relative number of same-sign to opposite-sign lepton pairs under the *Z* boson mass peak in data and MC, resulting in a 16% relative uncertainty. The uncertainty is assigned on $WZ/W\gamma^*$ in the 3ℓ-0SFOS category, and top, *Z*+jets and *WW* in the same-sign 2ℓ channel. The uncertainty labelled as 'Photon conversion rate' is assigned to the $W\gamma$ process in the same-sign 2ℓ channel, and is evaluated comparing the yield in data and in MC for events with two muons and one electron with no hit on the innermost pixel detector layer. It is relevant only for the same-sign 2ℓ categories and has a size of 6.5% on the $W\gamma$ background. The 'Pile-up' field of Table 9 includes the uncertainty on the weights applied to all simulated events to match the distribution of the number of pileup interactions to that of data. It is assigned by measuring the impact of an overall ±10%

scaling of this distribution. The uncertainty on the integrated luminosity for the 2012 data is ± 2.8%. It is derived, following the same methodology as that detailed in Ref. [68], from a preliminary calibration of the luminosity scale derived from beam-separation scans performed in November 2012. For the 2011 data the uncertainty on the integrated luminosity is ± 1.8% [68]. The dominant systematic uncertainties on the VH signal in the 4ℓ and 3ℓ channels are due to uncertainties on lepton reconstruction and on the jet energy scale and resolution. In the 2ℓ channels, the jet energy scale and resolution uncertainties are the most important.

(a) Uncertainties on the signal (%)

Channel	4ℓ		3ℓ			2ℓ		
Category	2SFOS	1SFOS	2SFOS	1SFOS	0SFOS	DFOS	SS2jet	SS1jet
Normalisation uncertainties								
NLO Acceptance	10	10	10	10	10	10	10	10
Higgs boson branch. fraction	4.1	4.0	4.0	3.9	3.7	4.2	4.2	3.9
QCD scale	3.1	3.1	1.5	1.2	1.2	1.7	1.0	1.0
PDFs and α_s	2.5	2.5	2.3	2.3	2.3	2.4	2.3	2.3
VH NLO EW corrections	2.1	2.1	2.0	2.0	2.0	2.1	2.1	2.1
Experimental uncertainties								
Jet	2.3	3.7	2.7	2.4	3.3	5.1	7.4	4.0
$E_{\mathrm{T}}^{\mathrm{miss}}$ Soft term	0.3	0.5	0.2	–	–	0.4	1.0	–
Electron	2.5	2.8	1.6	2.3	2.3	1.6	1.6	1.4
Muon	2.6	2.4	3.7	3.1	2.9	0.9	2.2	3.7
Trigger efficiency	0.2	0.1	0.4	0.3	0.3	0.5	0.6	0.5
b-tagging efficiency	0.9	0.8	0.9	0.8	0.8	2.9	3.5	2.6
Pile-up	2.0	0.5	1.7	2.1	1.5	2.4	0.9	3.2
Luminosity	2.8	2.8	2.8	2.8	2.8	2.8	2.8	2.8

(b) Uncertainties on the background (%)

Normalisation uncertainties								
QCD scale	0.3	0.2	1.0	0.9	–	3.7	13	1.5
PDFs and α_s	0.2	2.3	0.1	0.1	1.2	1.4	0.5	0.6
VVV K factor	2.8	8.1	1.1	1.9	0.5	–	–	–
MC modelling	5.2	4.3	7.1	6.6	–	4.1	0.2	0.3
CR statistics	8.1	6.6	4.2	3.9	8.8	2.5	2.8	3.5
Experimental uncertainties								
Jet	3.7	2.5	4.3	1.9	3.9	9.7	4.7	2.3
$E_{\mathrm{T}}^{\mathrm{miss}}$ Soft term	2.5	0.8	0.8	1.0	0.5	1.1	0.3	0.1
Electron	1.4	1.4	0.5	0.4	1.1	1.9	1.6	0.7
Muon	1.2	1.2	1.8	0.6	0.7	2.3	0.5	1.5
Trigger efficiency	–	0.2	0.2	–	–	0.1	–	–
b-tagging efficiency	0.6	0.7	0.6	0.8	2.5	0.7	1.4	0.4
Fake factor	–	–	–	–	–	3.2	11	12
Charge mis-assignment	–	–	–	–	1.4	–	0.6	0.6
Photon conversion rate	–	–	–	–	–	–	1.1	0.9
Pile-up	1.6	0.7	1.1	0.7	0.9	0.9	0.3	1.3
Luminosity	0.4	0.8	0.1	0.2	0.7	–	0.7	0.3

Table 9: Theoretical and experimental uncertainties, in %, on the predictions of (a) signal and (b) background for each analysis category. The dash symbol (–) indicates that the corresponding uncertainties either do not apply or are negligible. The values are post-fit and given for the 8 TeV data analysis for each signal category. Similar values are obtained for the 7 TeV data analysis. The values indicated with a "–" symbol are negligible.

8 Results

The number of events in each of the analysed categories is summarised in Table 10 for both the 8 TeV and 7 TeV data samples. In the 2ℓ-DFOS and 2ℓ-SS1jet categories the observed events are slightly larger than the expectation. The lepton flavour composition of the events is shown in Table 11 where the high event yield of the 2ℓ-SS1jet category mainly distributes in the $\mu\mu$ and μe channels. Several checks were performed in order to exclude that the excess was caused by failures of the detector subsystems in particular data acquisition periods and that known detector defects were not increasing the expected rate of particular background sources. Moreover, the kinematic distributions of the events were analysed in order to look for striking features pointing to some particular missing background contribution. Because no particular problem was observed, the data excess was attributed to statistical fluctuations.

Distributions of some of the relevant variables in the event selection are presented for 8 TeV data in Figure 6 for the 4ℓ and 3ℓ analyses and in Figure 7 for the 2ℓ analyses. Figures 6 (a) and 6 (c) show the opening angle between the leptons in the Higgs boson candidate's frame, $\Delta\phi^{\text{boost}}_{\ell_0\ell_1}$, in 4ℓ-1SFOS events. Figures 6 (b) and 6 (d) show the $\Delta\phi^{\text{boost}}_{\ell_0\ell_1}$ in 4ℓ-2SFOS events. Figure 6 (e) presents the BDT score distribution in 3ℓ-2SFOS and 3ℓ-1SFOS signal regions and Figure 6 (f) shows the distribution of ΔR computed between the leptons from the Higgs boson candidate, $\Delta R_{\ell_0\ell_1}$, in the 3ℓ-0SFOS signal region. Figure 6 (a) and 6 (b) are obtained applying the selections in Table 5.2 only down to the cuts on the p^{miss}_T, in order to retain some statistics, while the full selection is applied to produce the distributions in Figures 6 (c) and 6 (d). The distributions in Figures 6 (e) and 6 (f) are shown with all the selections applied but for the one on the variable on view. Figure 7 (a) presents the transverse mass, m_T, in the 2ℓ-DFOS SR, Figure 7 (b) the smallest opening angle in transverse plane between a lepton and a jet in the 2ℓ-SS1jet SR, $\Delta\phi^{min}_{\ell,jet}$, and Figure 7 (c) $\Delta\phi^{min}_{\ell,jet}$ in the 2ℓ-SS2jet SR. The distributions in Figure 7 are shown with all the selections applied but for the one on the variable on view. No data populates Figure 6 (c). In all the other distributions good agreement between data and MC prediction is observed.

Process	4ℓ		3ℓ			2ℓ		
Category	2SFOS	1SFOS	2SFOS	1SFOS	0SFOS	DFOS	SS2jet	SS1jet
Higgs								
$VH\,(H \to WW^*)$	0.208 ± 0.025	0.235 ± 0.029	0.73 ± 0.10	1.61 ± 0.18	1.43 ± 0.16	2.15 ± 0.24	1.04 ± 0.17	2.04 ± 0.28
$VH\,(H \to \tau\tau)$	0.0126 ± 0.0036	0.0087 ± 0.0030	0.057 ± 0.010	0.152 ± 0.022	0.248 ± 0.034	—	0.0365 ± 0.0080	0.270 ± 0.035
ggF	—	—	0.076 ± 0.015	0.085 ± 0.018	—	2.43 ± 0.49	—	—
VBF	—	—	—	—	—	0.180 ± 0.025	—	—
ttH	—	—	—	—	—	—	—	—
Background								
V	—	—	0.22 ± 0.16	1.87 ± 0.62	0.37 ± 0.15	13.7 ± 3.6	7.9 ± 3.7	14.9 ± 4.8
VV	1.17 ± 0.20	0.306 ± 0.059	19.2 ± 3.0	27.5 ± 4.1	4.70 ± 0.57	10.1 ± 1.6	11.2 ± 2.1	26.3 ± 3.7
VVV	0.117 ± 0.044	0.102 ± 0.036	0.80 ± 0.28	2.15 ± 0.74	2.93 ± 0.29	—	—	0.467 ± 0.049
Top	0.014 ± 0.011	—	0.91 ± 0.26	2.43 ± 0.63	3.72 ± 0.91	23.9 ± 3.9	0.75 ± 0.19	1.34 ± 0.51
Others	—	—	—	—	—	2.31 ± 0.95	0.71 ± 0.30	0.60 ± 0.24
Total	1.30 ± 0.25	0.41 ± 0.10	21.1 ± 3.6	34.0 ± 6.0	11.7 ± 1.8	49.9 ± 5.4	20.6 ± 4.6	43.6 ± 6.1
Observed events	0	3	22	38	14	63	25	62

Process	4ℓ		3ℓ			2ℓ		
Higgs								
$V(H \to WW^*)$	0.0226 ± 0.0028	0.0208 ± 0.0025	0.129 ± 0.014	0.325 ± 0.034	0.291 ± 0.030	0.285 ± 0.041		
$V(H \to \tau\tau)$	0.0031 ± 0.0011	0.00145 ± 0.00074	0.0163 ± 0.0035	0.0411 ± 0.0063	0.0670 ± 0.0095	0.0075 ± 0.0031		
ggF	—	—	0.0452 ± 0.0015	0.0106 ± 0.0050	0.0048 ± 0.0027	0.322 ± 0.090		
VBF	—	—	—	—	—	0.0212 ± 0.0038		
ttH	—	—	—	0.0061 ± 0.0040	0.0041 ± 0.0032	—		
Background								
V	—	—	0.36 ± 0.30	0.59 ± 0.34	0.36 ± 0.22	3.4 ± 1.3		
VV	0.37 ± 0.13	0.031 ± 0.012	4.08 ± 0.64	5.7 ± 1.0	1.32 ± 0.20	0.89 ± 0.54		
VVV	0.0140 ± 0.0011	0.00952 ± 0.00095	0.082 ± 0.028	0.207 ± 0.071	0.338 ± 0.031	—		
Top	0.0055 ± 0.0040	—	0.12 ± 0.14	0.44 ± 0.27	0.44 ± 0.29	3.18 ± 0.76		
Others	—	—	—	—	—	—		
Total	0.39 ± 0.14	0.041 ± 0.013	4.6 ± 1.1	7.0 ± 1.9	2.46 ± 0.66	7.5 ± 1.7		
Observed events	1	0	5	6	2	7		

Table 10: Number of observed and predicted events in the SRs and their composition in the (a) 8 TeV and (b) 7 TeV data analyses. Background processes that contribute less than 1% of the total background, and Higgs boson production mechanisms that contribute less than 1% of the VH signal, are not included in the table. The uncertainties on event yields include both statistical and systematic components (see section 7)

Process	SS 2ℓ (ee)		SS 2ℓ (eμ)		SS 2ℓ (μe)		SS 2ℓ (μμ)	
Category	2jet	1jet	2jet	1jet	2jet	1jet	2jet	1jet
Higgs								
$VH\,(H \to WW^*)$	0.154 ± 0.067	0.390 ± 0.084	0.355 ± 0.080	0.50 ± 0.12	0.243 ± 0.083	0.69 ± 0.14	0.285 ± 0.063	0.46 ± 0.10
$VH\,(H \to \tau\tau)$	0.0088 ± 0.0045	0.063 ± 0.013	0.0119 ± 0.0040	0.081 ± 0.018	0.0040 ± 0.0020	0.080 ± 0.014	0.0118 ± 0.0042	0.046 ± 0.010
ggF	0.0028 ± 0.0021	0.0011 ± 0.0011	—	—	—	—	—	—
VBF	—	—	—	—	—	—	—	—
ttH	—	—	—	—	—	—	—	—
Background								
V	2.9 ± 2.8	5.0 ± 2.0	2.5 ± 1.0	6.6 ± 2.3	1.37 ± 0.62	2.09 ± 0.70	1.14 ± 0.79	1.14 ± 0.82
VV	2.78 ± 0.90	6.3 ± 1.3	4.7 ± 1.3	10.9 ± 1.8	2.33 ± 0.67	5.6 ± 1.1	1.33 ± 0.35	3.52 ± 0.76
VVV	—	—	—	—	—	0.133 ± 0.023	—	0.113 ± 0.027
Top	0.123 ± 0.076	0.49 ± 0.14	0.36 ± 0.15	0.48 ± 0.23	0.238 ± 0.081	0.389 ± 0.133	0.035 ± 0.032	—
Others	0.069 ± 0.036	—	0.26 ± 0.12	0.44 ± 0.17	0.32 ± 0.15	—	0.061 ± 0.031	0.056 ± 0.029
Total	5.9 ± 3.1	11.9 ± 2.4	7.9 ± 1.7	18.6 ± 3.0	4.26 ± 0.94	8.2 ± 1.3	2.60 ± 0.90	4.8 ± 1.2
Observed events	4	12	8	25	7	14	6	11

Table 11: Number of observed and predicted events in the SS 2ℓ SRs in 8 TeV data analysis with different lepton flavour combinations: *ee*, *eμ*, *μe* and *μμ*. Background processes that contribute less than 1% of the total background, and Higgs boson production mechanisms that contribute less than 1% of the VH signal, are not included in the table. The uncertainties on event yields include both statistical and systematic components (see section 7)
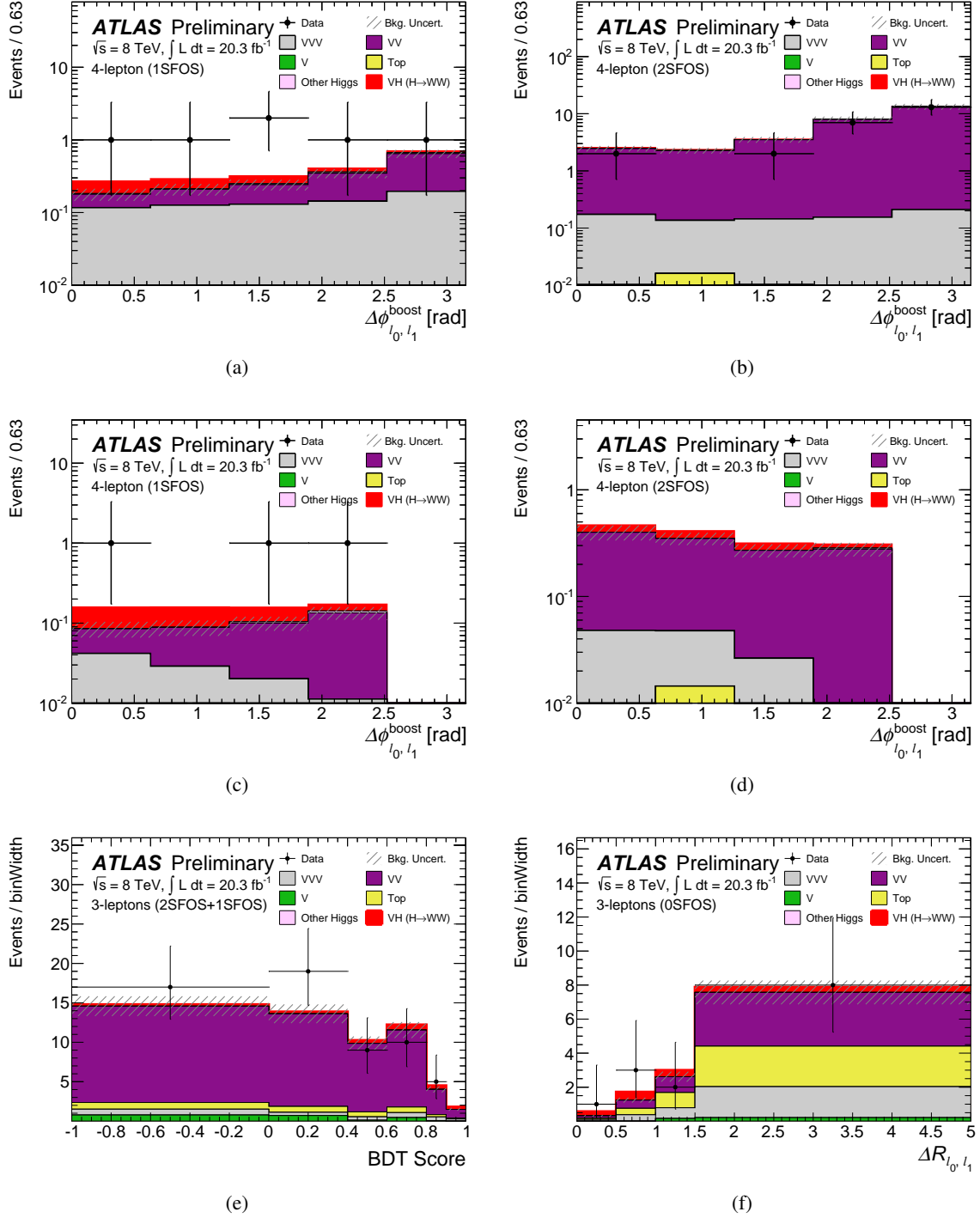
Figure 6: Distributions of relevant quantities for the 4ℓ and 3ℓ analyses, using 8 TeV data: (a) and (c) $\Delta\phi_{\ell_0\ell_1}^{boost}$ with 4ℓ-1SFOS events, (b) and (d) $\Delta\phi_{\ell_0\ell_1}^{boost}$ with 4ℓ-2SFOS events, (e) BDT score in 3ℓ-2SFOS plus 3ℓ-1SFOS SR and (f) $\Delta R_{\ell_0\ell_1}$ in 3ℓ-0SFOS SR. Figures (a) and (b) are obtained applying the cuts down to the p_T^{miss} selection from the top in Table 5.2, removing the other selections in order to increase the otherwise very limited statistics, while on the distributions in (c) and (d) all the selections are applied. The distributions in (e) and (f) are shown with all the selections applied but for the one on the variable on view . Data (dots) are compared to the background plus VH (m_H=125 GeV) signal expectation (stacked filled histograms), where the background components are normalised as discussed in section 6. The hatched area on the histogram represents the total uncertainty, which includes the systematic and the statistical ones, on the total background estimate. 26
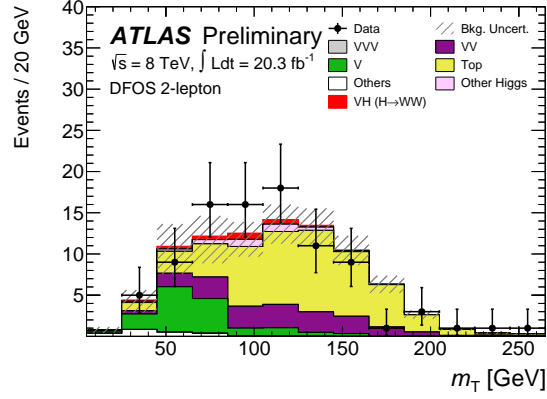
(a)
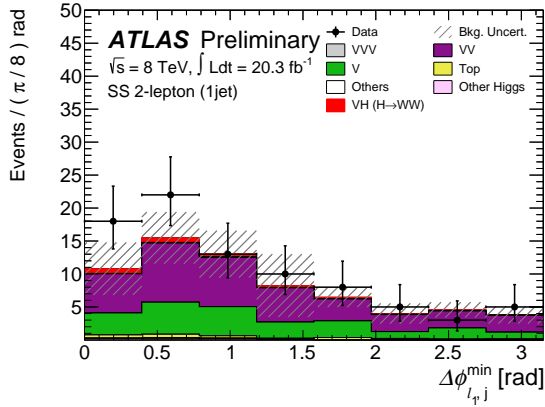
(b)
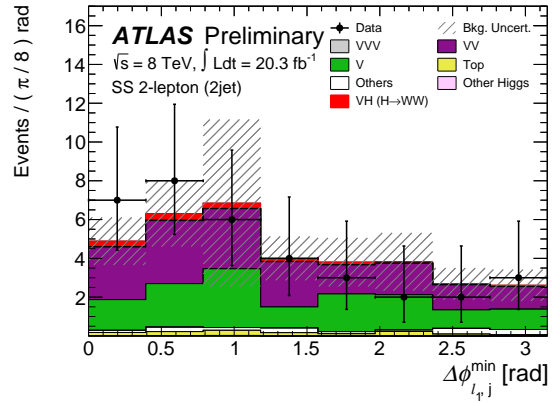
(c)

Figure 7: Distributions of relevant quantities for the 2ℓ analyses, using 8 TeV data: (a) m_T in 2ℓ-DFOS SR, (b) $\Delta\phi^{min}_{\ell,jet}$ and (c) $\Delta\phi^{min}_{\ell,jet}$ in 2ℓ-SS2jet SR. The distributions are shown with all the selections applied but for the one on the variable on view. Data (dots) are compared to the background plus VH (m_H=125 GeV) signal expectation from simulation (stacked filled histograms), where the background components are normalised as discussed in section 6. The hatched area on the histogram represents the total uncertainty, which includes the systematic and the statistical ones, on the total background estimate.

9 Statistical Interpretation

The data collected at $\sqrt{s}$ = 7 TeV and 8 TeV have been combined in all analysed categories in order to search for the Higgs boson in the *WH* and *ZH* production modes and to extract information on their combination. The analysis has been optimised for the search of the associated production of a Higgs boson with mass near m_H = 125 GeV. For such mass the Higgs bosons selected by this analysis are mainly decaying to $WW^* \rightarrow \ell\nu + X$, but a small contamination of $H \rightarrow \tau\tau \rightarrow \ell\nu\ell\nu$ from the *VH* production mode is present. The $H \rightarrow \tau\tau$ is included in the background yield and it is normalised using the SM expectation for the *VH* production cross section (σ_{VH}) and the $H \rightarrow \tau\tau$ branching fraction ($\mathrm{Br}(H \rightarrow \tau\tau)$).

The signal yields are extracted using the profile likelihood ratio method [69] that consists in maximising a binned likelihood function $\mathcal{L}(\mu, \theta \mid n)$. The likelihood is the product of Poisson distributions for each signal and control region. The mean values of the distributions are the sum of the expected yields of signal and background. The symbol n represents the observed events in each signal and control region. The signal and background expectations are function of the signal strength parameter, μ, and a set of nuisance parameters, θ. The signal strength μ multiplies the SM predicted signal event yield of each category, while background normalisation factors, included as nuisance parameters, represent corrections for background sources normalised to data. Signal and background predictions depend on systematic uncertainties that are described by nuisance parameters. The normalization factors are left free in the fit, while the constraints for the systematic uncertainties are chosen to be log-normal distributions.

The test statistic q_μ is defined as

$$q_\mu = -2\ln\frac{\mathcal{L}(\mu, \hat{\hat{\theta}}_\mu)}{\mathcal{L}_{\mathrm{max}}} = -2\ln\Lambda, \tag{1}$$

The symbol $\hat{\hat{\theta}}_\mu$ indicates the nuisance parameter values at the maximum of the likelihood for a given μ. The denominator is the maximum value of $\mathcal{L}$ obtained floating both μ and θ. When the denominator is maximized, μ takes the value of $\hat{\mu}$. The p_0 value is computed for the test statistic q_0, from eq. 1 evaluated at $\mu = 0$, and is defined to be the probability to obtain a value of q_0 larger than the observed value under the background-only hypothesis. There are no bounds on $\hat{\mu}$, although q_0 is defined to be negative if $\hat{\mu} \leq 0$. The equivalent formulation, expressed in terms of the number of standard deviations, σ, is referred to as the local significance Z_0. The signal acceptance for all production modes and decays is computed assuming a SM Higgs boson with mass m_H = 125.36 GeV [70], corresponding to the statistics and systematics weighted combination of the masses measured in the $H \rightarrow \gamma\gamma$ and $H \rightarrow 4\ell$ decay channels by ATLAS. The acceptance for this mass results from an interpolation between the acceptances computed assuming a SM Higgs boson mass of 125 GeV and of 130 GeV.

The expected sensitivity to a SM Higgs boson with mass m_H = 125.36 GeV, the observed significance for $H \rightarrow WW^*$ decays and the measured μ value using the categories described in section 5 are given in Table 12. The 3ℓ-2SFOS and 3ℓ-1SFOS categories are further split in the likelihood function according to the value of the BDT score, while the 3ℓ-0SFOS category is split in intervals of $\Delta R_{\ell_0, \ell_1}$, as discussed in section 5.2.2. The intervals are shown in Figures 6 (e) and 6 (f) respectively. Each of the 2ℓ-SS2jet and 2ℓ-SS1jet category is further split into four sub-categories according to the flavour of the leading and sub-leading leptons. For the 2ℓ-DFOS a single category is considered. The ggF and VBF contributions are included into the signal contribution and the relative strengths of the *VH*, ggF and VBF productions are fixed to the SM values and constrained with their theoretical uncertainties.

The *VH* data are then combined with the ggF/VBF categories in the $H \rightarrow WW^* \rightarrow \ell\nu\ell\nu$ decay channel described in Ref. [22]. The combination is again performed building a likelihood function that includes the signal and control regions of the analyses related to the three production modes. The detector and theoretical systematic uncertainties affecting the same sources are correlated among different

Category	Signal significance Z_0			Observed signal strength μ_{obs}					
	Exp. Z_0	Obs Z_0	Obs. Z_0	μ	Tot. err. +	Tot. err. −	Syst. err. +	Syst. err. −	μ
4ℓ	0.44	1.9		4.9	4.6	3.1	1.2	0.35	
2SFOS	0.31	0		−5.9	6.8	4.1	0.33	0.72	
1SFOS	0.40	2.5		9.6	8.1	5.4	2.1	0.64	
3ℓ	0.84	0.66		0.72	1.3	1.1	0.42	0.27	
1SFOS and 2SFOS	0.57	0		−2.9	3.2	3.2	2.1	2.5	
0SFOS	0.69	1.2		1.6	1.9	1.4	0.51	0.29	
2ℓ	0.61	2.0		3.7	1.9	1.8	1.2	1.4	
DFOS	0.57	1.1		2.2	2.0	1.9	1.1	1.0	
SS2jet	0.24	1.4		7.7	6.0	5.5	3.2	3.3	
SS1jet	0.63	2.3		8.4	4.3	3.8	2.3	2.0	

Table 12: The signal significance Z_0, and the $H \to WW^*$ signal strength μ evaluated in the signal regions of the analysed categories, combining 7 TeV and 8 TeV data. The expected (exp.) and observed (obs.) values are shown. The two plots represent the observed significance and the observed μ. In the μ plot the statistical uncertainty (stat.) is represented by the thick line, the total uncertainty (tot.) by the thin line. All values are computed for a Higgs boson mass of 125.36 GeV.

analyses. The signal strengths that normalise the yields expected for each production mode are correlated in all categories while the background normalisation factors are uncorrelated among the different analyses as they cover different phase spaces. The VH-specific results are assessed considering the ggF and VBF processes as background and treating their uncertainties as nuisance parameters.
The fit results for the signal strength for the WH, ZH and VH production processes are respectively:

$$\mu_{WH} = 2.1^{+1.5}_{-1.3}\,(\text{stat.})^{+1.2}_{-0.8}\,(\text{sys.}), \quad \mu_{ZH} = 5.1^{+3.8}_{-3.0}\,(\text{stat.})^{+1.9}_{-0.9}\,(\text{sys.}),$$

$$\mu_{VH} = 3.0^{+1.3}_{-1.1}\,(\text{stat.})^{+1.0}_{-0.7}\,(\text{sys.})$$

Figure 8 shows the likelihood as a function of μ_{WH} and μ_{ZH} and indicates no significant correlation between the two measured variables.

Table 13 summarises the signal strengths for each production mode and their combination at a value of $m_H = 125.36$ GeV, together with the observed and the expected significance. The combined value is $\mu = 1.16^{+0.16}_{-0.15}(\text{stat.})^{+0.18}_{-0.15}(\text{sys.})$ and no $H \to WW^*$ hypothesis is rejected at the observed (expected) significance of 6.5 (5.9) σ. Figure 9 shows the likelihood scan as a function of each production mode signal strength separately and of the combined signal strength.

The obtained values are all compatible with the SM expectation within 1.4 standard deviations. Figures 10 (a) and (b) show the two-dimensional dependence of the likelihood from μ_{VH} and μ_{ggF}, and from μ_{VH} and μ_{VBF}. The signal strength that is not shown is kept as a free unconstrained parameter in the fit. As shown, the correlation among the several parameters is seen to be small. The central values obtained for μ_{ggF} and μ_{VBF} are slightly different from those reported in [22]. The shift represents a few percent of the quoted errors and is ascribed to the presence of a small contamination of VH events in the 1-jet and 2-jets categories of the ggF and VBF analysis and is pulled up by the rates observed in the VH-targeted categories.
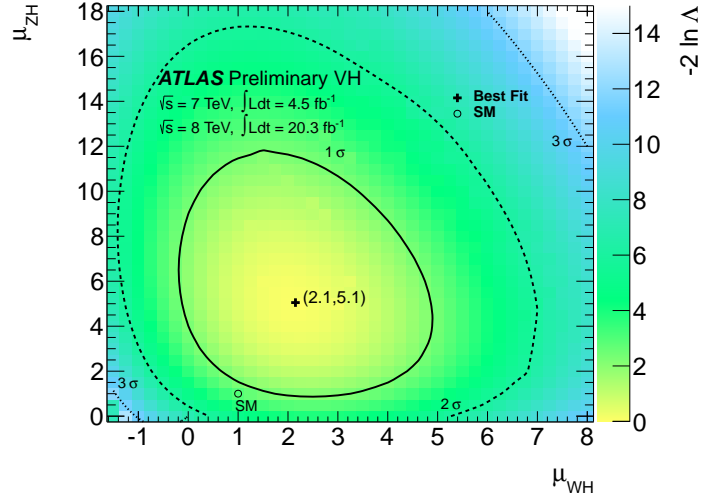
Figure 8: The likelihood as a function of μ_{WH} and μ_{ZH}, for $m_H = 125.36\,\text{GeV}$. The contours correspond to the values of (μ_{WH}, μ_{ZH}) associated with the 68%, 90% and 95% confidence levels, respectively. The markers indicate the best fit to the data and the SM expectation $(\mu_{WH}, \mu_{WH})=(1,1)$.
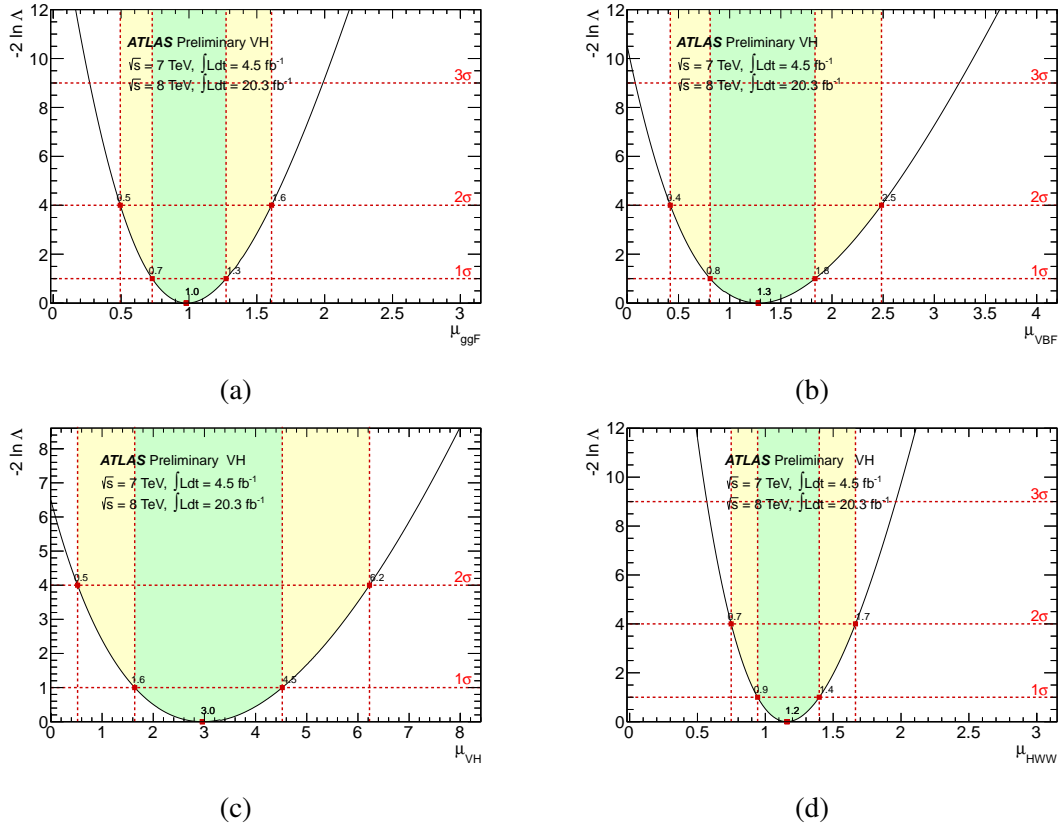

Figure 9: The likelihood as a function of the μ value from the different production processes (a) ggF, (b) VBF, (c) VH and (d) their combination. All values are extracted from the combined fit. The best fit values are represented by the markers at the likelihood minima, with the $\pm 1\sigma$ and $\pm 2\sigma$ uncertainties given by the green and yellow shaded bands, respectively.

	Signal significance Z_0				Observed signal strength μ_{obs}					
Category	Exp. Z_0	Obs. Z_0	Obs. Z_0		μ	Tot. err. +	Tot. err. −	Syst. err. +	Syst. err. −	μ
ggF	4.4	4.2			0.98	0.29	0.26	0.22	0.18	
VBF	2.6	3.2			1.28	0.55	0.47	0.32	0.25	
VH	0.93	2.5			3.0	1.6	1.3	0.95	0.65	
WH only	0.77	1.4			2.1	1.9	1.6	1.2	0.79	
ZH only	0.30	2.0			5.1	4.3	3.1	1.9	0.89	
ggF+VBF+VH	5.9	6.5			1.16	0.24	0.21	0.18	0.15	

Table 13: The signal significance Z_0, and the signal strength μ evaluated for the different production modes: ggF, VBF and *VH* (*WH* and *ZH*) for a Higgs boson mass of 125.36 GeV, for the 7 TeV and 8 TeV data combined.
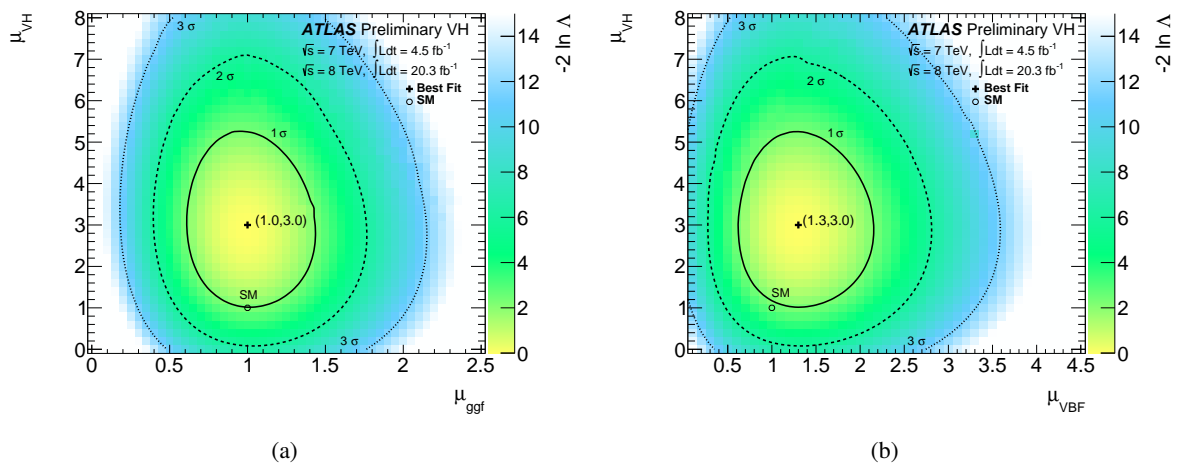
Figure 10: Likelihood as a function of the production mode signal strengths in two-dimensional planes of (a) μ_{VH} vs μ_{ggF} and (b) μ_{VH} vs μ_{VBF}. The markers indicate the best fit to the data and the SM expectation (1,1).

Measurement of the couplings to fermions and vectors (k_V, k_F)

The values of μ_{ggF}, μ_{VBF} and μ_{VH} can be used to test the consistency of the fermionic and bosonic couplings of the Higgs boson with the SM prediction using the formalism developed in Ref. [21]. Assuming the validity of the SU(2) custodial symmetry and a universal scaling of the fermion couplings with respect to their SM prediction, two parameters are defined: the scale factor for the SM coupling to the vector bosons (k_V) and the scale factor for the coupling to the fermions (k_F). Loop-induced processes are assumed to scale as expected from the SM. In this parametrisation the total width of the Higgs boson can be expressed as the sum of the different partial widths, each one rescaled by the square of the appropriate scaling factor. Neglecting the small contribution from $\Gamma(H \to \gamma\gamma)$ and rarer decay modes, the branching fraction to the WW^* pair can be expressed as:

$$Br(H \to WW^*) = \frac{k_V^2 \Gamma_{\text{SM}}(H \to WW^*)}{k_F^2 \Gamma_{\text{SM}}(H \to f\bar{f}) + k_F^2 \Gamma_{\text{SM}}(H \to gg) + k_V^2 \Gamma_{\text{SM}}(H \to VV)},$$

where $\Gamma_{\text{SM}}(H \to f\bar{f})$, $\Gamma_{\text{SM}}(H \to gg)$ and $\Gamma_{\text{SM}}(H \to VV)$ are the SM partial decay widths to fermions, gluons and vector bosons respectively.

The gluon fusion process depends directly on the fermion scale factor k_F^2 through the top and bottom quark loops, while the VBF and $qq \to VH$ production cross sections are proportional to k_V^2, as expressed by the following relations

$$\sigma(gg \to H) = k_F^2 \sigma_{\text{SM}}(gg \to H), \quad \sigma(qq \to Hqq) = k_V^2 \sigma_{\text{SM}}(qq \to Hqq),$$

$$\sigma(qq \to WH, ZH) = k_V^2 \sigma_{\text{SM}}(qq \to WH, ZH).$$

and the $gg \to ZH$ production cross sections are more complex functions of both k_F and k_V [71]

$$\sigma(gg \to ZH)_{8 \text{ TeV}} = (0.37 \times k_F^2 - 1.64 \times k_F \times k_V + 2.27 \times k_V^2)\, \sigma_{\text{SM}}(gg \to ZH)_{8 \text{ TeV}},$$

$$\sigma(gg \to ZH)_{7 \text{ TeV}} = (0.35 \times k_F^2 - 1.58 \times k_F \times k_V + 2.24 \times k_V^2)\, \sigma_{\text{SM}}(gg \to ZH)_{7 \text{ TeV}},$$

where the σ without subscript indicates the k_V, k_F dependent cross sections and σ_{SM} represents the SM cross sections. The signal event yield is expressed as $\sigma \cdot Br(H \to WW^*)$ using the narrow width approximation. Only the relative sign between k_F and k_V is observable and hence in the following only $k_V > 0$ is considered, without loss of generality.

Sensitivity to the sign results from negative interference between the box diagram in which both the Z and H bosons are produced directly from the heavy quark loop and the triangle diagram in which only the Z^* is produced and subsequently radiates a H boson [72]. Because the relative weights of such processes depends on the $\sqrt{s}$ of the interaction, different coefficients are available for 7 and 8 TeV.

The likelihood dependence from k_V and k_F is shown in Figure 11. The product $\sigma(gg \to H) \cdot Br(H \to WW^*)$, which is measured with high accuracy, does not depend on $|k_F|$ in the limit $|k_F| \gg k_V$. This explains the low sensitivity to high values of k_F. On the other hand μ_{VBF} and μ_{VH}, as measured for the Higgs boson decay to WW^*, should vanish in the limit $|k_F| \gg k_V$ due to the increased value of the Higgs boson total width and the consequent reduction of the branching fraction to WW^* bosons. The observation of significant excesses in the latter modes therefore leads to an exclusion of the $|k_F| \gg k_V$ region.

The fit to the data results in two local minima and, although the negative k_F solution is preferred to the positive one at 0.5σ, the observed results are compatible with the SM expectation with the best fit values being:

$$|k_F| = 0.85^{+0.26}_{-0.20} \quad |k_V| = 1.06^{+0.10}_{-0.10}$$

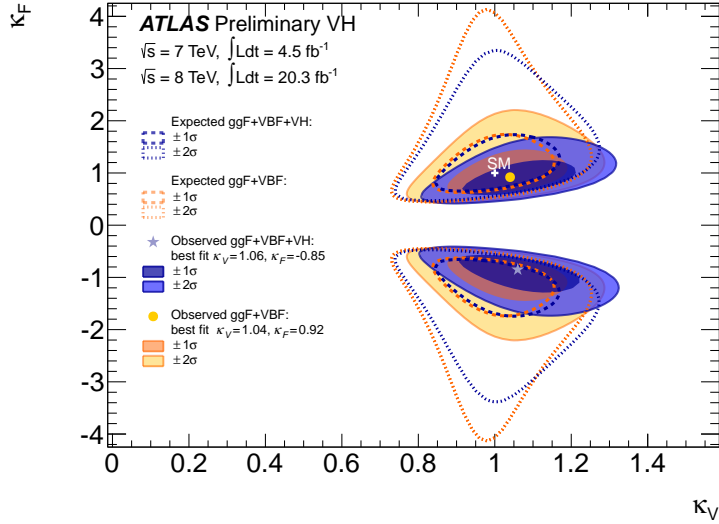and their correlation is $\rho = 0.54$.

Figure 11: The likelihood scan as a function of k_V and k_F both with and without the *VH* contribution. Both the expected and observed contours corresponding to the 68%, and 90% C.L. are shown. The markers indicate the best fit to the data and the SM expectation (k_V, k_F)=(1,1).

10 Conclusions

A search for the Standard Model Higgs boson produced in association with a *W* or *Z* boson and decaying into WW^* has been presented. The *WH* associated production is studied in the final states in which the three *W* bosons decay to leptons or where one *W* boson decays to hadrons while the others decay leptonically. The four lepton final state is used to search for the *ZH* production. The dataset corresponds to integrated luminosities of 4.5 fb^{-1} and 20.3 fb^{-1} recorded by the ATLAS experiment during Run 1 of the LHC proton-proton collisions at $\sqrt{s} = 7$ TeV and 8 TeV, respectively. For a Higgs boson mass of 125.36 GeV, the observed (expected) deviation from the background-only hypothesis (that includes the Standard Model expectation for $H \rightarrow \tau\tau$) corresponds to a significance of 2.5 (0.9) standard deviations. The ratio of the measured signal yield to its Standard Model expectation for *VH* production is found to be $\mu_{\mathrm{VH}} = 3.0^{+1.3}_{-1.1}$ (stat.)$^{+1.0}_{-0.7}$ (sys.). A combination with the gluon-gluon fusion and vector boson fusion analyses using the $H \rightarrow WW^* \rightarrow \ell\nu\ell\nu$ decay has also been presented. Including the *VH* production channel the observed significance for a Higgs boson decaying to WW^* is 6.5 σ with an expectation of 5.9 σ for a Standard Model Higgs boson of mass $m_H = 125.36$ GeV. The combined signal strength is $\mu = 1.16^{+0.16}_{-0.15}$(stat.)$^{+0.18}_{-0.15}$(sys.). The data have been analysed using a model where all Higgs boson's couplings to the vector bosons are scaled by a common factor k_V and those to the fermions by the factor k_F. They are measured as $|k_F| = 0.85^{+0.26}_{-0.20}$ and $|k_V| = 1.06^{+0.10}_{-0.10}$, with a correlation $\rho = 0.54$. The sensitivity to k_V is mainly dominated by the ggF and VBF production modes while the impact on the k_F measurement of the categories designed for the *VH* search is sizeable.

11 References

[1] F. Englert and R. Brout, *Broken symmetry and the mass of gauge vector mesons*, Phys. Rev. Lett. **13** (1964) 321–323.

[2] P. W. Higgs, *Broken symmetries and the masses of gauge bosons*, Phys. Rev. Lett. **13** (1964) 508–509.

[3] G. Guralnik, C. Hagen, and T. Kibble, *Global conservation laws and massless particles*, Phys.Rev.Lett. **13** (1964) 585–587.

[4] ATLAS Collaboration, *Observation of a new particle in the search for the Standard Model Higgs boson with the ATLAS detector at the LHC*, Phys. Lett. B **716** (2012) 1–29, `arXiv:1207.7214 [hep-ex]`.

[5] CMS Collaboration, *Observation of a new boson at a mass of 125 GeV with the CMS experiment at the LHC*, Phys. Lett. B **716** (2012) 30–61, `arXiv:1207.7235 [hep-ex]`.

[6] ATLAS Collaboration, *Measurements of Higgs boson production and couplings in diboson final states with the ATLAS detector at the LHC*, Phys. Lett. B **726** (2013) 88–119, `arXiv:1307.1427 [hep-ex]`.

[7] ATLAS Collaboration, *Evidence for the spin-0 nature of the Higgs boson using ATLAS data*, Phys.Lett. B **726** (2013) 120–144, `arXiv:1307.1432 [hep-ex]`.

[8] ATLAS Collaboration, *Measurements of fiducial and differential cross sections for Higgs boson production in the diphoton decay channel at $\sqrt{s}$ = 8 TeV with ATLAS*, JHEP **1409** (2014) 112, `arXiv:1407.4222 [hep-ex]`.

[9] ATLAS Collaboration, *Fiducial and differential cross sections of Higgs boson production measured in the four-lepton decay channel in pp collisions at $\sqrt{s}$ = 8 TeV with the ATLAS detector* , Phys. Lett. B **738** (2014) 234–253, `arXiv:1408.3226 [hep-ex]`.

[10] CMS Collaboration, *Observation of a new boson with mass near 125 GeV in pp collisions at $\sqrt{s}$ = 7 and 8 TeV*, JHEP **1306** (2013) 081, `arXiv:1303.4571 [hep-ex]`.

[11] CMS Collaboration, *Precise determination of the mass of the Higgs boson and tests of compatibility of its couplings with the standard model predictions using proton collisions at 7 and 8 TeV*, `arXiv:1412.8662 [hep-ex]`.

[12] CMS Collaboration, *Constraints on the spin-parity and anomalous HVV couplings of the Higgs boson in proton collisions at 7 and 8 TeV*, `arXiv:1411.3441 [hep-ex]`.

[13] T. Aaltonen and others, CDF and D0 Collaborations, *Higgs boson studies at the Tevatron*, Phys. Rev. D **88** (2013) 052014, `arXiv:1303.6346 [hep-ex]`. `http://link.aps.org/doi/10.1103/PhysRevD.88.052014`.

[14] CMS Collaboration, *Search for the standard model Higgs boson produced in association with a W or a Z boson and decaying to bottom quarks*, Phys. Rev. D **89** (2014) 012003, `arXiv:1310.3687 [hep-ex]`. `http://link.aps.org/doi/10.1103/PhysRevD.89.012003`.

[15] ATLAS Collaboration, *Search for the $b\bar{b}$ decay of the Standard Model Higgs boson in associated (W/Z)H production with the ATLAS detector*, JHEP **1501** (2015) 069, `arXiv:1409.6212 [hep-ex]`.

[16] ATLAS Collaboration, *Measurement of Higgs boson production in the diphoton decay channel in pp collisions at center-of-mass energies of 7 and 8 TeV with the ATLAS detector*, Phys.Rev. **D90** (2014) 112015, `arXiv:1408.7084 [hep-ex]`.

[17] ATLAS Collaboration, *Measurements of Higgs boson production and couplings in the four-lepton channel in pp collisions at center-of-mass energies of 7 and 8 TeV with the ATLAS detector*, Phys.Rev. **D91** (2015) 012006, `arXiv:1408.5191 [hep-ex]`.

[18] CMS Collaboration, *Observation of the diphoton decay of the Higgs boson and measurement of its properties*, Eur.Phys.J. **C74** (2014) 3076, `arXiv:1407.0558 [hep-ex]`.

[19] CMS Collaboration, *Measurement of the properties of a Higgs boson in the four-lepton final state*, Phys.Rev. **D89** (2014) 092007, `arXiv:1312.5353 [hep-ex]`.

[20] CMS Collaboration, *Measurement of Higgs boson production and properties in the WW decay channel with leptonic final states*, JHEP **1401** (2014) 096, `arXiv:1312.1129 [hep-ex]`.

[21] S. Heinemeyer et al., *Handbook of LHC Higgs Cross Sections: 3. Higgs Properties*, `arXiv:1307.1347 [hep-ph]`.

[22] ATLAS Collaboration, *Observation and measurement of Higgs boson decays to WW* with the ATLAS detector*, `arXiv:1412.2641 [hep-ex]`.

[23] ATLAS Collaboration, *The ATLAS Experiment at the CERN Large Hadron Collider*, JINST **3** (2008) S08003.

[24] J. M. Butterworth, J. R. Forshaw, and M. H. Seymour, *Multiparton interactions in photoproduction at HERA*, Z. Phys. **C72** (1996) 637–646.

[25] H.-L. Lai, M. Guzzi, J. Huston, Z. Li, P. M. Nadolsky, et al., *New parton distributions for collider physics*, Phys.Rev. **D82** (2010) 074024.

[26] P. M. Nadolsky et al., *Implications of CTEQ global analysis for collider observables*, Phys. Rev. **D78** (2008) 013004.

[27] A. Sherstnev and R. S. Thorne, *Parton distributions for the LHC*, Eur. Phys. J **C55** (2009) 553.

[28] S. Dittmaier et al., *Handbook of LHC Higgs Cross Sections: 1. Inclusive Observables*, `arXiv:1101.0593 [hep-ph]`.

[29] S. Dittmaier et al., *Handbook of LHC Higgs Cross Sections: 2. Differential Distributions*, `arXiv:1201.3084 [hep-ph]`.

[30] M. Ciccolini, S. Dittmaier, and M. Kramer, *Electroweak radiative corrections to associated WH and ZH production at hadron colliders*, Phys.Rev. **D68** (2003) 073003, `arXiv:hep-ph/0306234 [hep-ph]`.

[31] O. Brein, A. Djouadi, and R. Harlander, *NNLO QCD corrections to the Higgs-strahlung processes at hadron colliders*, Phys.Lett. **B579** (2004) 149–156, `arXiv:hep-ph/0307206 [hep-ph]`.

[32] A. Denner, S. Dittmaier, S. Kallweit, and A. Muck, *EW corrections to Higgs strahlung at the Tevatron and the LHC with HAWK*, PoS **EPS-HEP2011** (2011) 235, `arXiv:1112.5258 [hep-ph]`.

[33] S. Catani, L. Cieri, G. Ferrera, D. de Florian, and M. Grazzini, *Vector boson production at hadron colliders: a fully exclusive QCD calculation at NNLO*, Phys.Rev.Lett. **103** (2009) 082001, `arXiv:0903.2120 [hep-ph]`.

[34] S. Catani and M. Grazzini, *An NNLO subtraction formalism in hadron collisions and its application to Higgs boson production at the LHC*, Phys.Rev.Lett. **98** (2007) 222002, `arXiv:hep-ph/0703012 [hep-ph]`.

[35] J. M. Campbell and R. Ellis, *MCFM for the Tevatron and the LHC*, Nucl.Phys.Proc.Suppl. **205-206** (2010) 10–15, `arXiv:1007.3492 [hep-ph]`.

[36] T. Binoth, G. Ossola, C. Papadopoulos, and R. Pittau, *NLO QCD corrections to tri-boson production*, JHEP **0806** (2008) 082, `arXiv:0804.0350 [hep-ph]`.

[37] ATLAS Collaboration, *The ATLAS Simulation Infrastructure*, Eur.Phys.J. **C70** (2010) 823–874, `arXiv:1005.4568 [physics.ins-det]`.

[38] S. Agostinelli et al., *GEANT4: A Simulation toolkit*, Nucl.Instrum.Meth. **A506** (2003) 250–303.

[39] ATLAS Collaboration, "*The simulation principle and performance of the ATLAS fast calorimeter simulation FastCaloSim.*" ATL-PHYS-PUB-2010-013, 2010. https://cds.cern.ch/record/1300517/.

[40] T. Sjostrand, S. Mrenna, and P. Z. Skands, *A Brief Introduction to PYTHIA 8.1*, Comput.Phys.Commun. **178** (2008) 852–867, `arXiv:0710.3820 [hep-ph]`.

[41] P. Nason, *A new method for combining NLO QCD with shower Monte Carlo algorithms*, JHEP **11** (2004) 040, `arXiv:hep-ph/0409146`.

[42] M. L. Mangano, M. Moretti, F. Piccinini, R. Pittau, and A. D. Polosa, *ALPGEN, a generator for hard multiparton processes in hadronic collisions*, JHEP **0307** (2003) 001, `arXiv:hep-ph/0206293 [hep-ph]`.

[43] G. Corcella, I. Knowles, G. Marchesini, S. Moretti, K. Odagiri, et al., *HERWIG 6: An Event generator for hadron emission reactions with interfering gluons (including supersymmetric processes)*, JHEP **0101** (2001) 010, `arXiv:hep-ph/0011363 [hep-ph]`.

[44] T. Gleisberg, S. Hoeche, F. Krauss, M. Schonherr, S. Schumann, et al., *Event generation with SHERPA 1.1*, JHEP **0902** (2009) 007, `arXiv:0811.4622 [hep-ph]`.

[45] S. Frixione and B. R. Webber, *Matching NLO QCD computations and parton shower simulations*, JHEP **0206** (2002) 029, `arXiv:hep-ph/0204244 [hep-ph]`.

[46] J. Alwall, P. Demin, S. de Visscher, R. Frederix, M. Herquet, et al., *MadGraph/MadEvent v4: The New Web Generation*, JHEP **0709** (2007) 028, `arXiv:0706.2334 [hep-ph]`.

[47] J. Alwall, M. Herquet, F. Maltoni, O. Mattelaer, and T. Stelzer, *MadGraph 5 : Going Beyond*, JHEP **1106** (2011) 128, `arXiv:1106.0522 [hep-ph]`.

[48] B. P. Kersevan and E. Richter-Was, *The Monte Carlo event generator AcerMC versions 2.0 to 3.8 with interfaces to PYTHIA 6.4, HERWIG 6.5 and ARIADNE 4.1*, Comput.Phys.Commun. **184** (2013) 919–985, `arXiv:hep-ph/0405247 [hep-ph]`.

[49] Binoth, T. and Kauer, N. and Mertsch, P., *Gluon-induced QCD corrections to $pp \to ZZ \to \ell\bar{\ell}\ell'\bar{\ell'}$* , `arXiv:0807.0024 [hep-ph]`.

[50] T. Binoth, M. Ciccolini, N. Kauer, and M. Kramer, *Gluon-induced W-boson pair production at the LHC*, JHEP **0612** (2006) 046, `arXiv:hep-ph/0611170 [hep-ph]`.

[51] ATLAS Collaboration, *Measurement of the muon reconstruction performance of the ATLAS detector using 2011 and 2012 LHC proton-proton collision data*, Eur.Phys.J. **C74** (2014) 3130, `arXiv:1407.3935 [hep-ex]`.

[52] ATLAS Collaboration, *Electron reconstruction and identification efficiency measurements with the ATLAS detector using the 2011 LHC proton-proton collision data*, Eur.Phys.J. **C74** (2014) 2941, `arXiv:1404.2240 [hep-ex]`.

[53] ATLAS Collaboration, "*Electron efficiency measurements with the ATLAS detector using the 2012 LHC proton-proton collision data.*" ATLAS-CONF-2014-032, 2014. http://cds.cern.ch/record/1706245.

[54] ATLAS Collaboration, "*Properties of Jets and Inputs to Jet Reconstruction and Calibration with the ATLAS Detector Using Proton-Proton Collisions at $\sqrt{s}$ = 7 TeV.*" ATLAS-CONF-2010-053, 2010. https://cds.cern.ch/record/1281310/.

[55] M. Cacciari, G. P. Salam, and G. Soyez, *The anti-k_t jet clustering algorithm*, JHEP **0804** (2008) 063, `arXiv:0802.1189 [hep-ph]`.

[56] ATLAS Collaboration, "*Commissioning of the ATLAS high-performance b-tagging algorithms in the 7 TeV collision data.*" ATLAS-CONF-2011-102, 2011. https://cds.cern.ch/record/1369219.

[57] ATLAS Collaboration, "*Calibration of the b-tagging efficiency for c jets with the ATLAS detector using events with a W boson produced in association with a single c quark.*" ATLAS-CONF-2013-109, 2013. https://cds.cern.ch/record/1640162/.

[58] ATLAS Collaboration, "*Calibration of the performance of b-tagging for c and light-flavour jets in the 2012 ATLAS data.*" ATLAS-CONF-2014-046, 2014. http://cds.cern.ch/record/1741020.

[59] ATLAS Collaboration, *Performance of Missing Transverse Momentum Reconstruction in Proton-Proton Collisions at 7 TeV with ATLAS*, Eur.Phys.J. **C72** (2012) 1844, `arXiv:1108.5602 [hep-ex]`.

[60] ATLAS Collaboration, "Pile-up Suppression in Missing Transverse Momentum Reconstruction in the ATLAS Experiment in Proton-Proton Collisions at sqrts = 8 TeV." ATLAS-CONF-2014-019, 2014. https://cds.cern.ch/record/1702055.

[61] ATLAS Collaboration, "*Measurement of the missing transverse momentum based on tracks in proton-proton collisions at sqrt(s) = 900 GeV centre-of-mass energy with the ATLAS detector.*" ATLAS-CONF-2010-020, 2010. https://cds.cern.ch/record/1277652.

[62] A. Hoecker et al., *TMVA - Toolkit for Multivariate Data Analysis*, `arXiv:physics/0703039 [physics]`.

[63] K. Hamilton, P. Nason, and G. Zanderighi, *MINLO: Multi-Scale Improved NLO*, JHEP **1210** (2012) 155, `arXiv:1206.3572 [hep-ph]`.

[64] F. Campanario, V. Hankele, C. Oleari, S. Prestel, and D. Zeppenfeld, *QCD corrections to charged triple vector boson production with leptonic decay*, Phys.Rev. **D78** (2008) 094012, `arXiv:0809.0790 [hep-ph]`.

[65] M. Botje, J. Butterworth, A. Cooper-Sarkar, A. de Roeck, J. Feltesse, et al., *The PDF4LHC Working Group Interim Recommendations*, arXiv:1101.0538 [hep-ph].

[66] ATLAS Collaboration, *Jet energy measurement and its systematic uncertainty in proton-proton collisions at $\sqrt{s}$ = 7 TeV with the ATLAS detector*, Eur.Phys.J. **C75** (2015) 17, arXiv:1406.0076 [hep-ex].

[67] ATLAS Collaboration, "*Calibration of b-tagging using dileptonic top pair events in a combinatorial likelihood approach with the ATLAS experiment.*" ATLAS-CONF-2014-004, 2014. https://cds.cern.ch/record/1664335.

[68] ATLAS Collaboration, *Improved luminosity determination in pp collisions at $\sqrt{s}$ = 7 TeV using the ATLAS detector at the LHC*, Eur.Phys.J. **C73** (2013) 2518, arXiv:1302.4393 [hep-ex].

[69] G. Cowan, K. Cranmer, E. Gross, and O. Vitells, *Asymptotic formulae for likelihood-based tests of new physics*, Eur.Phys.J. **C71** (2011) 1554, arXiv:1007.1727 [physics.data-an].

[70] ATLAS Collaboration, *Measurement of the Higgs boson mass from the $H \rightarrow \gamma\gamma$ and $H \rightarrow ZZ^* \rightarrow 4\ell$ channels with the ATLAS detector using 25 fb^{-1} of pp collision data*, Phys.Rev. **D90** (2014) 052004, arXiv:1406.3827 [hep-ex].

[71] ATLAS Collaboration, "*Measurements of the Higgs boson production and decay rates and coupling strengths using pp collision data at $\sqrt{s}$ = 7 and 8 TeV in the ATLAS experiment.*" ATLAS-CONF-2015-07, 2015. https://cds.cern.ch/record/1988426.

[72] C. Englert, M. McCullough, and M. Spannowsky, *Gluon-initiated associated production boosts Higgs physics*, Phys. Rev. **D89** (2014) 013013, arXiv:1310.4828 [hep-ph].